HHS Public Access

Author manuscript

ACS Nano. Author manuscript; available in PMC 2021 January 28.

Published in final edited form as:

ACS Nano. 2020 January 28; 14(1): 255–271. doi:10.1021/acsnano.9b03978.

Stromal Modulation and Treatment of Metastatic Pancreatic Cancer with Local Intraperitoneal Triple miRNA/siRNA Nanotherapy

Ying Xie[#], **Yu Hang**[#], **Yazhe Wang**, **Richard Sleightholm**, **Dipakkumar R. Prajapati**
University of Nebraska Medical Center, Omaha, Nebraska

Johannes Bader
University of Nebraska Medical Center, Omaha, Nebraska, and Ludwig-Maximilians-Universität München, Munich, Germany

Ao Yu, **Weimin Tang**
University of Nebraska Medical Center, Omaha, Nebraska

Lee Jaramillo
University of Nebraska Medical Center, Omaha, Nebraska, and Bohemica Pharmaceuticals, LLC, La Vista, Nebraska

Jing Li, **Rakesh K. Singh**, **David Oupický**
University of Nebraska Medical Center, Omaha, Nebraska

Abstract

Nanomedicines achieve tumor-targeted delivery mainly through enhanced permeability and retention (EPR) effect following intravenous (IV) administration. Unfortunately, the EPR effect is severely compromised in pancreatic cancer due to hypovascularity and dense desmoplastic stroma. Intraperitoneal (IP) administration may be an effective EPR-independent local delivery approach to target peritoneal tumors. Besides improved delivery, effective combination delivery strategies are needed to improve pancreatic cancer therapy by targeting both cancer cells and cellular interactions within the tumor stroma. Here, we described simple cholesterol-modified polymeric

Corresponding Author: david.oupicky@unmc.edu.
[#]Y.X. and Y.H. contributed equally.

Author Contributions

Y.X., Y.H., and Y. W. performed *in vitro* and *in vivo* experiments. R.S. performed ultrasound imaging. D.P. and R.K.S. analyzed tissue sections. J.B., A.Y., W.T., L.J., and J.L. helped with *in vitro* or *in vivo* studies. R.K.S. edited the manuscript. Y.X. and D.O. wrote the manuscript. D.O. conceived and supervised the study. All authors discussed the results and commented on the manuscript.

Supporting Information

The Supporting Information is available free of charge at https://pubs.acs.org/doi/10.1021/acsnano.9b03978.
Synthesis and characterization of PCX, CXCR4 antagonism assay, CXCR4 expression of cancer cells, cytotoxicity of PCX, characterization of nanoparticles, cellular uptake and intracellular trafficking of nanoparticles, miR-210 expression in PSCs, stability of nanoparticles against ascites and mouse serum, peritoneal retention of nanoparticles, biodistribution of nanoparticles 4 h after injection, fluorescence images of tumor sections, biodistribution of nanoparticles in healthy mice, tumor mesothelium in KPC mice and human patient, ultrasound analysis of primary tumor growth, metastasis in tissues/organs after treatment with nanoparticles, histology analysis of tumor sections, whole blood analysis, kidney and liver function analysis (PDF)

Complete contact information is available at: https://pubs.acs.org/10.1021/acsnano.9b03978

The authors declare the following competing financial interest(s): Drs. Oupicky and Li are cofounders and coowners of Bohemica Pharmaceuticals, LLC.

CXCR4 antagonist (PCX) nanoparticles (to block cancer-stroma interactions) for codelivery of anti-miR-210 (to inactivate stroma-producing pancreatic stellate cells (PSCs)) and siKRAS^{G12D} (to kill pancreatic cancer cells). IP administration delivered the nanoparticles to an orthotopic syngeneic pancreatic tumors as a result of preferential localization to the tumors and metastases with disrupted mesothelium and effective tumor penetration. The local IP delivery resulted in nearly 15-fold higher tumor accumulation than delivery by IV injection. Through antagonism of CXCR4 and downregulation of miR-210/KRAS^{G12D}, the triple-action nanoparticles favorably modulated desmoplastic tumor microenvironment via inactivating PSCs and promoting the infiltration of cytotoxic T cells. The combined therapy displayed improved therapeutic effect when compared with individual therapies as documented by the delayed tumor growth, depletion of stroma, reduction of immunosuppression, inhibition of metastasis, and prolonged survival. Overall, we present data that a local IP delivery of a miRNA/siRNA combination holds the potential to improve pancreatic cancer therapy.

Graphical Abstract

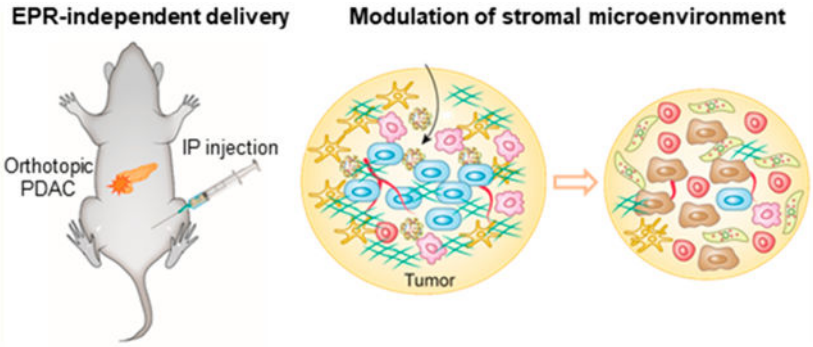

Keywords

intraperitoneal administration; tumor stroma; immunosuppression; metastasis; CXCR4; miRNA-210; pancreatic cancer

Pancreatic ductal adenocarcinoma (PDAC) is among the most lethal human malignancies with a 5-year survival of less than 8%.[1,2] After decades of efforts to develop better therapeutic approaches, conventional chemotherapy regimens offer only modest benefits.[3] The failure of the current PDAC treatments has been in part due to their focus on cancer cells without sufficient attention to the role of tumor stroma in PDAC progression. Dense desmoplastic stroma is one of the hallmarks of PDAC.[4] Activated pancreatic stellate cells (PSCs) are key drivers of desmoplasia via their production of excessive extracellular matrix (ECM) components. Intricate PDAC stroma crosstalk regulates tumor cell growth, invasion, metastasis, and immune escape through tumor–stroma interactions.[5,6] Moreover, the hypovascularity of the nearly impenetrable desmoplastic stroma severely hampers conventional vascular delivery of therapeutics into tumors, which further contributes to the treatment failures.[7] Depletion of stromal desmoplasia has been reported to improve PDAC therapy.[8,9] However, some preclinical and clinical studies raise concerns that extensive stromal depletion in PDAC may promote tumor progression, metastasis, and reduce survival

because of the elimination of critical stromal components needed for tissue homeostasis.[6,10,11] Nevertheless, due to the key role of stroma in PDAC, targeting of cancer cells, stroma, and cancer cell–stroma interactions is a promising approach for the development of improved therapies.

Nanoscale vectors have been widely used to deliver drugs and nucleic acids to tumors of various origins. These nanomedicines are typically injected intravenously (IV) into the body and then rely on extravasation through leaky tumor blood vessels to accumulate in the tumors based on the so-called enhanced permeability and retention (EPR) effect.[12] Unfortunately, poor extravasation in the hypovascular PDAC tumors combined with the systemic capture by the mononuclear phagocytic system (MPS) compromises the EPR effect and results in suboptimal delivery of nanomedicines.[13,14] Some studies have reported strategies to overcome the stromal barriers in PDAC by engineering the carrier systems, but that often leads to complexity that diminishes translational potential.[15,16] Local delivery represents a potential strategy to overcome these limitations in PDAC drug delivery, but there is a lack of versatile local delivery systems.[17] Intraperitoneal (IP) delivery has been recently proposed as an alternative administration strategy to deliver nanomedicines to peritoneal tumors including PDAC.[18] IP delivery may maximize local efficacy while limiting systemic side effects. IP injection can improve the retention of nanomedicines in the peritoneal cavity and provide more opportunities for direct contact of tumors with high therapeutic concentrations.[19] It is believed that IP injected particles localize to peritoneal tumors instead of normal organs due to differences in the surface mesothelium. Abdominal organs are covered by peritoneum with intact mesothelium and submesothelial fibrous connective tissue, which act as barriers against the adhesion and entry of nanoparticles through the surface of the organs.[20] In contrast, peritoneal tumors usually are devoid of these surface coverings due to the disruption of peritoneal mesothelial cells during tumor progression as a result of the interactions of cancer cells with the peritoneum.[21–23] The tumor targeting ability of IP-injected nanoparticles is also affected by the physicochemical properties like surface charge, size, and presence of targeting ligands.[24–26] Overall, local delivery by IP administration provides an effective alternative to IV administration and holds potential for tumor-specific localization of nanoparticles in PDAC.

PDAC is characterized by hypoxia, which affects both cancer cells and PSCs present in the tumor. Hypoxia stimulates PSCs to induce fibrosis and promote desmoplasia.[27,28] MicroRNAs (miRNAs) are involved in the activation of PSCs.[29] For example, hypoxia induces the overexpression of miR-210, which regulates multiple related signaling pathways, needed for better adaptation of the cells to the severe hypoxic environment.[30] MiR-210 regulates cancer cell proliferation, apoptosis, and metastasis.[31] Silencing of miR-210 in PSCs with miRNA inhibitor (anti-miR) can modulate PDAC stroma through PSC inactivation.

Mutations of KRAS are key drivers of the tumor initiation, progression, and metastasis.[32,33] Inhibition of the oncogenic KRAS with genetic manipulation inhibits PDAC progression in mice,[34] but there are no clinically effective small-molecule KRAS inhibitors available.[35] Small interfering RNA (siRNA) targeting $KRAS^{G12D}$ is an effective alternative to small-

molecule KRAS inhibitors, and its use has been shown to improve overall survival in mouse models of PDAC.[36,37]

The chemokine receptor CXCR4 and its primary ligand CXCL12 regulate cancer development through tumor–stroma interactions. CXCL12 is secreted, among others, by activated PSCs, and when it binds to CXCR4 on cancer cells, it activates multiple intracellular signaling pathways that promote migration and invasion.[38] CXCR4/CXCL12 is also involved in cancer immune invasion by decreasing the tumor infiltration of cytotoxic $CD8^+$ T-lymphocytes.[39,40] Inhibitors targeting the CXCR4/CXCL12 axis can block tumor–stroma interactions and demonstrate therapeutic effect in PDAC through inhibition of metastasis and augmentation of T cell immunotherapy.[39,41,42]

Despite the strong biological rationale for the combined CXCR4/miR-210/siKRAS^{G12D} therapy of PDAC, such an approach is severely limited by the physical barriers posed by the PDAC desmoplasia. In the present study, we describe the development of a local delivery system for combination triple miRNA/siRNA nanotherapy based on our previously described polymeric CXCR4 antagonist (PCX).[43,44] PCX was synthesized from a CXCR4 antagonist AMD3100 and conjugated with cholesterol to enhance the efficacy of the EPR-independent delivery. Because of the critical roles of miR-210, KRAS^{G12D}, and CXCR4/CXCL12 axis in PDAC, we hypothesized that combining silencing of miR-210/KRAS^{G12D} and blockade of CXCR4 would cooperatively enhance the PDAC therapy through PSC inhibition, targeting cancer cells, and inhibiting tumor–stroma interactions in pancreatic tumors (Scheme 1). To test this hypothesis, we prepared PCX nanoparticles coloaded with anti-miR-210 and siKRAS^{G12D} and studied the efficacy of local IP delivery by comparing their tumor delivery efficacy with IV injection. We further evaluated the effect of the treatment on pancreatic tumor microenvironment and therapeutic outcomes in a murine orthotopic PDAC model with dense desmoplasia.

RESULTS AND DISCUSSION

Inhibition of CXCR4 and Delivery of miRNA/siRNA Combination by PCX *in Vitro*.

AMD3100 is a cyclam-based CXCR4 antagonist that specifically inhibits CXCR4/CXCL12 signaling. We have utilized the cationic character of AMD3100 to synthesize PCX polycations that maintain the CXCR4 inhibitory properties while being able to encapsulate various nucleic acids in the form of nanosized particles (polyplexes). In this study, nondegradable PCX was synthesized by Michael addition copolymerization of AMD3100 with hexamethylene bis(acrylamide). The parent PCX was covalently modified with an optimized amount of cholesterol to improve the *in vivo* stability and effectiveness of the IP delivery of the PCX/RNA nanoparticles (Figure S1A).[42,43,45] The composition and molecular weight of PCX were characterized by 1H NMR and size exclusion chromatography. The PCX used in the present study had a weight-average molecular weight M_w of 14.4 kg/mol and cholesterol weight content of 16.7% (Figure S1B,C).

CXCR4 antagonism of PCX was validated using a CXCR4 receptor redistribution assay (Figure S2). PCX displayed a dose-dependent CXCR4 antagonism with complete inhibition observed at 2 μg/mL (~140 nM). Negative control polyethylenimine (PEI) showed no

CXCR4 inhibition, which excluded the possibility that CXCR4 antagonism of PCX is due to nonspecific electrostatic binding of polycations to the negatively charged active site of the CXCR4 receptor.

Prior to examining encapsulation of the anti-miR/siRNA combination, we evaluated the ability of PCX to inhibit migration of mouse and human PDAC cells. Surface expression of CXCR4 receptor was first confirmed in murine KPC8060 cells (32.7% $CXCR4^+$) and human COLO357 cells (55.6% $CXCR4^+$) (Figure S3). To minimize the potential effect of PCX cytotoxicity on cell migration, we used 2 μg/mL as a safe PCX concentration (Figure S4). AMD3100 (300 nM) was used as a positive control. As shown in Figure 1A, CXCL12 induced migration of both KPC8060 and COLO357 cells. Both PCX and AMD3100 showed nearly complete inhibition of the migration of KPC8060 cells at the tested concentrations. Both PCX and AMD3100 also exhibited strong inhibitory activity in the human COLO357 cells. Control PEI failed to inhibit migration of either of the used cell lines.

The ability of PCX to form nanoparticles and encapsulate a combination of anti-miR and siRNA was evaluated with agarose gel electrophoresis. The nanoparticles were prepared by mixing various amounts of PCX with a mixture of anti-miR/siRNA containing equal molar concentrations of the two RNAs. PCX fully condensed the anti-miR/siRNA mixture at and above PCX/(anti-miR+siRNA) w/w ratios of 2 (Figure 1B). Nanoparticles showed sizes of ~57 nm with a dispersity index of 0.12 according to the dynamic light scattering measurement (Figure 1C). The ζ potential was 19 mV (Figure S5A). The nanoparticles presented as uniform particles with a mostly spherical morphology based on observation using transmission electron microscopy (TEM) and atomic force microscopy (AFM) (Figure 1D,E). Heparin displacement assay was used to evaluate the release of anti-miR and siRNA from the nanoparticles. Nanoparticles completely released the anti-miR and siRNA combination above 160 μg/mL heparin (Figure S5B). Since poor stability in the presence of serum and nucleases may limit the *in vivo* application of RNA, the stability of the nanoparticles against serum and RNase I was analyzed using gel electrophoresis. In comparison with a mixture of naked anti-miR and siRNA, PCX nanoparticles improved the stability of anti-miR/siRNA against both serum and RNase I degradation (Figure S5C).

We next examined the efficacy of the nucleic acid delivery to PDAC cells *in vitro*. Since anti-miR and siRNA share similar physiochemical properties, we prepared the PCX nanoparticles using only the siRNA. Fluorescently labeled PCX (AF647-PCX) and siRNA (FAM-siRNA) were used in this study to visualize the uptake, intracellular distribution, and particle disassembly in KPC8060 cells. Both AF647-PCX (red) and FAM-siRNA (green) were observed internalized in the cells, demonstrating effective uptake of the nanoparticles. Separation of PCX and siRNA fluorescence signals in the cells indicated a disassembly of a large portion of the nanoparticles (Figure 1F). Flow cytometry analysis showed that 86% of the KPC8060 cells internalized both PCX and siRNA (Figure S6A). Endosomal escape of the nanoparticles in KPC8060 was studied by staining endo/lysosomes with LysoTrackerRed. The fluorescence of the FAM-siRNA (green) was found mostly colocalized with endolysosomes (red) after incubation for 2 h. After 6 h, FAM-siRNA localized predominantly in the cytoplasm with only a limited extent of colocalization with the endo/lysosomes (Figure S6B). This result confirmed endosomal escape of the

nanoparticles in KPC8060 cells. Similar effective cellular uptake and endosomal escape of nanoparticles were also found in human COLO357 cells (Figure S7). Lastly, we analyzed the penetration of the PCX nanoparticles into 3D multicellular tumor spheroids prepared from KPC8060 cells. The penetration was evaluated by measuring the fluorescence of FAM-siRNA with confocal microscopy of the spheroids and flow cytometry of single cell suspension prepared from the spheroids. PCX/FAM-siRNA nanoparticles showed effective tumor-penetrating ability as suggested by the observed internalization in 76% of the cells in the tumor spheroids (Figure 1G and Figure S7D).

Inhibition of Both Cancer Cells and Pancreatic Stellate Cells by Codelivery of Anti-miR-210/siKRAS^{G12D} *in Vitro*.

After reaching the cytoplasm, therapeutic anti-miR and siRNA can downregulate targeted miRNA and mRNA, respectively. The efficacy of the delivery was assessed from the silencing of the target RNA using nanoparticles coloaded with anti-miR-210 and siKRAS^{G12D}. Control nanoparticles with negative control anti-miR-NC and siNC were also used. PDAC cells were treated with the PCX nanoparticles, and expression of miR-210 and KRAS^{G12D} mRNA was measured using qRT-PCR. Treatment with PCX/(anti-miR-210+siNC) nanoparticles significantly downregulated the miR-210 expression (~51% decrease) in KPC8060 cells but did not affect the KRAS expression. Likewise, PCX/(anti-miR-NC+siKRAS^{G12D}) nanoparticles reduced KRAS^{G12D} mRNA levels (~40% decrease) but did not affect miR-210 expression. Only treatment with PCX/(anti-miR-210+siKRAS^{G12D}) nanoparticles downregulated both miR-210 and KRAS^{G12D} mRNA levels (Figure 2A). Reduction of both miR-210 and KRAS^{G12D} mRNA levels was also found in human COLO357 cells after treatment with the PCX/(anti-miR-210+siKRAS^{G12D}) nanoparticles (Figure 2B). Similarly, inhibition of CXCR4 alone (PCX/(anti-miR-NC +siNC)) did not affect the expression of either miR-210 or KRAS.

Next, we studied the anticancer activity of the nanoparticles in PDAC cells. The effect of the nanoparticles on PDAC cell apoptosis was analyzed by staining the cells with DAPI and evaluating their nuclear morphology (Figure 2C and Figure S8A). Upon treatment with PCX/(anti-miR-210+siK-RAS^{G12D}), more than 40% of the KPC8060 cells were apoptotic. Nanoparticles with only single active RNA (PCX/(anti-miR-210+siNC) and PCX/(anti-miR-NC+siKRAS^{G12D})) only induced apoptosis in ~9% and ~14% cells, respectively. The observed combined pro-apoptotic effect of the PCX/(anti-miR-210+siKRAS^{G12D}) nanoparticles was also found in the human COLO357 cells. These findings were validated by a cell viability assay (Figure 2D). PCX/(anti-miR-210+siK-RAS^{G12D}) nanoparticles exhibited significantly higher cell killing (~66%) in KPC8060 cells than PCX/(anti-miR-210+siNC) nanoparticles (~30%) and PCX/(anti-miR-NC +siKRAS^{G12D}) nanoparticles (~45%). PCX/(anti-miR-210+siKRAS^{G12D}) nanoparticles demonstrated a similar enhanced combined killing effect in the COLO357 cells. Colony formation assay was used to evaluate the tumorigenic potential of cancer cells after treatment with the nanoparticles (Figure 2E). Treatment with PCX/(anti-miR-210+siK-RAS^{G12D}) reduced colony formation in KPC8060 cells by ~70%. This inhibition effect was significantly higher than that of PCX/(anti-miR-210+siNC) nanoparticles (~38%) and PCX/(anti-miR-NC+siKRAS^{G12D}) (~38%). The combination PCX/(anti-miR-210+siKRAS^{G12D}) nanoparticles also inhibited colony

formation in human COLO357 cells. Overall, results from the comprehensive *in vitro* anticancer activity studies confirmed the combined anticancer activity of PCX/(anti-miR-210+siKRAS^{G12D}) nanoparticles in pancreatic cancer cells through downregulation of both miR-210 and KRAS^{G12D} while indicating no direct cytotoxic effect of the CXCR4 inhibition.

We then studied the treatment effect on cultured human PSCs by qRT-PCR and immunofluorescence (IF) staining of fibrosis markers. As shown in Figure S8B, significant downregulation of miR-210 expression was only observed in PSCs cells after treatment with PCX/(anti-miR-210+siNC) and PCX/(anti-miR-210+siKRAS^{G12D}) nanoparticles. As shown in Figure 2F, activated PSCs (untreated G1 group) expressed high levels of α-smooth muscle actin (αSMA) and collagen I. The silencing of miR-210 by PCX/(anti-miR-210+siNC) and PCX/(anti-miR-210+siKRAS^{G12D}) nanoparticles significantly decreased the expression of both αSMA and collagen I in the human PSCs, indicating inactivation of PSCs by the combined CXCR4 inhibition and miR-210 downregulation. As expected, delivery of siKRAS^{G12D} failed to contribute to the inactivation of the PSCs.

Thus, the above *in vitro* studies confirmed that silencing miR-210 and KRAS^{G12D} by the PCX nanoparticles leads to combined anticancer activity in PDAC cells through inducing apoptosis and decreasing tumorigenesis. The nanoparticles also effectively inactivated human PSCs *in vitro* through miR-210 inhibition. Although the anticancer activity of the individual anti-miR-210 and siKRAS^{G12D} has been reported previously,[36,46] the molecular mechanism behind their effective combination in cancer cells and PSCs requires further studies.

Improved Delivery of Nanoparticles to Orthotopic Pancreatic Tumor/Metastasis through IP Injection.

KPC8060 cells with mutant KRAS^{G12D} and p53 were orthotopically implanted in the tail of the pancreas of immunocompetent C57BL/6 mice to establish orthotopic PDAC model. This model mimics human disease with similar oncogene expression, tumor growth characteristics, metastasis profile, and desmoplastic stroma reaction.[10,36] Small pancreatic tumors with limited metastases, except for local splenic invasion, were found as early as 2–3 weeks after cell implantation. Large primary tumors and widespread metastasis were observed after 4–5 weeks (Figure S9).

Protein binding and stability in biological media are important factors in determining the *in vivo* fate of nanoparticles.[47] Before *in vivo* analysis of the nanoparticles, we studied their protein binding and stability in ascites and serum obtained from mice with established KPC8060 tumors. PCX nanoparticles showed pronounced protein binding in both ascites and mouse serum. However, the extent of protein binding was much lower than in the case of control PEI particles. The abundant protein binding reversed the surface charge of the nanoparticles to negative values. Importantly, PCX nanoparticles showed minimal signs of disassembly or aggregation upon protein binding, exhibited good colloidal stability with particle size maintained below 100 nm, and protected anti-miR/siRNA against ascites/serum degradation (Figure S10).

We first compared IP and IV administration of the nanoparticles in terms of the plasma circulation time. Equal doses of AF647-PCX/FAM-siRNA nanoparticles were injected either IV or IP in the PDAC tumor-bearing mice. The AF647-PCX fluorescence intensity in blood was normalized by setting intensity at 2 min after IV injection as 100% (Figure 3A,B). After IV injection, the blood fluorescence signal decreased rapidly to ~18% at 1 h postinjection, and the signal almost disappeared by 24 h due to fast clearance of the nanoparticles from the blood. Prolonged peritoneal retention and limited systemic absorption are important for effective IP treatment.[48] When evaluating the peritoneal retention of IP-injected nanoparticles, we observed widespread local retention of the nanoparticles at 4 h postinjection. The observed amount was significantly reduced after 24 h (Figure S11). Nanoparticles are expected to be absorbed into the blood from the peritoneal cavity.[19] The diameter of the lymphatic ducts in the peritoneal cavity is about 1 μm.[49] Nanoparticles may further pass through lymph nodes and enter blood.[50] The properties of the PCX nanoparticles, even with the ascites proteins bound, suggested that they would be susceptible to clearance from the peritoneal cavity mainly as a result of lymphatic drainage.[49] As expected, the content of the nanoparticles in blood increased after IP injection and reached ~17% at 1 h, which was followed by a complete clearance at 24 h. The fluorescence intensity in blood after IP injection is a function of absorption from the peritoneal cavity and MPS clearance from the blood. We estimated the area under the curve (AUC) for both IV and IP administration and found that $AUC_{0-\infty}$ of the IP injection was ~67% of the AUC observed in the IV injection. The results suggested that a significant portion of the IP-injected nanoparticles was retained in the peritoneum and not absorbed into the blood circulation.

To study the biodistribution of the nanoparticles, AF647-PCX/FAM-siRNA was injected IV or IP in mice with orthotopic pancreatic tumors. Following animal sacrifice at 4 and 24 h post injection, we measured the fluorescence of the AF647-PCX in the isolated tissues. In the mice given IV injection, the nanoparticles mainly accumulated in the liver and showed poor distribution into tumors at both 4 and 24 h after injection. The nanoparticles were also found in the spleen and the lungs (Figure S12 and Figure 3C–E). In the animals given IP injection, significant accumulation of the nanoparticles in the orthotopic tumors was observed. Mean fluorescence intensity (MFI) of AF647-PCX in the tumors was nearly five-fold higher than in the case of the IV treatment at 4 h postinjection. The relative tumor accumulation in the IP group further increased with time, reaching nearly a 15-fold higher level relative to the IV group at 24 h (Figure 3C–E). In comparison with the IV group, the IP injected animals also showed substantially decreased hepatic and splenic accumulation of the nanoparticles, most likely due to lower clearance by the MPS. Since an estimated 67% of the IP injected nanoparticles were absorbed into the systemic circulation, it is interesting that the hepatic distribution in the IP group was only 20% of the IV group. Besides the limitations of fluorescence in quantifying biodistribution of nanoparticles,[51] IP administration may result in engaging different metabolic routes, different protein adsorption profile, and faster biliary excretion in comparison with IV injection,[52] which could lead to lower liver accumulation of IP-injected nanoparticles.

To obtain detailed information about the distribution of the nanoparticles within the tumors, frozen tumor sections were analyzed using confocal microscopy. Both AF647-PCX (red)

and FAM-siRNA (green) fluorescence were present in the tumors of IP-injected mice, suggesting delivery of assembled nanoparticles (Figure 3F). Importantly, the nanoparticles were delivered to both peripheral and central regions of the pancreatic tumors. We observed pronounced nanoparticle localization on the tumor surfaces but limited perivascular distribution, which suggested that the nanoparticles penetrated the tumors directly from the peritoneal cavity without any significant contribution of the blood-circulating particles (Figure S13A). At higher magnification, we observed that only the polymer fluorescence but not the siRNA was found in the nucleus (Figure S13B). These results show that the polymers, rather than whole nanoparticles, enter the nucleus. After 24 h of administration, a part of the nanoparticles disassembles and frees the polymers and siRNA. The size and properties of the free polycations allowed them to cross nuclear pores (~5 nm), while the nanoparticles (~57 nm) failed to do so.[53] In addition to the cancer cells within the tumors, the nanoparticles were also found in activated PSCs, which expressed αSMA (Figure S13C). Only weak AF647-PCX and FAM-siRNA fluorescence were found in the tumors of animals treated with the IV injection (Figure 3F). Moreover, we observed the distribution of the nanoparticles in the peritoneal metastatic lesions. A significant increase in the distribution of the nanoparticles was found in local splenic invasion compared with normal spleen and healthy pancreas (Figure 3G and Figure S14). These results confirmed the superior capability of the IP-injected nanoparticles to deliver PCX and the RNA combination to pancreatic tumors and peritoneal metastases.

To explore the reasons for the high tumor accumulation of the PCX nanoparticles, we analyzed tumor surface peritoneum as a barrier for IP delivered nanoparticles.[19,23] We examined the HE stained tissue slides of normal organs, primary pancreatic tumors, and metastases in various organs including liver, kidney, spleen, diaphragm, and lung. We found that, as compared to the normal organs like pancreas and kidney, primary pancreatic tumors and other organs containing metastatic foci lacked the visceral peritoneum that is normally composed of flat mesothelial cells (mesothelium/mesothelial lining). In some instances, we observed the presence of a fibrous capsule. Some metastatic organs (e.g., liver) showed broken mesothelial lining. In comparison with normal organs, tumors lacked a layer of compact mesothelial cells, which likely contributed to the tumor localization of the nanoparticles (Figure 3H). The characteristic lack of mesothelium on the tumor surfaces was observed not only in orthotopically implanted tumors but also in spontaneously developed tumors in genetically engineered KPC mice and in human PDAC patient samples (Figure S15), suggesting applicability and clinical translatability of the findings to human medicine.

To evaluate if CXCR4-dependent tumor uptake was involved in the observed findings, we have preinjected the animals with anti-CXCR4 antibody to block the CXCR4 receptor in the tumor before nanoparticles injection. Biodistribution of the IP injected nanoparticles in the mice with CXCR4 blockade was compared with that in mice without the blockade. We found that the blockade of CXCR4 receptor did not reduce the tumor localization of the IP injected nanoparticles (Figure 3I). This result demonstrates that tumor accumulation of the IP injected nanoparticles is independent of the CXCR4 receptor binding.

Dense stromal desmoplasia is a physical barrier for delivery of nanomedicines in PDAC. Hypovascular pancreatic tumors limit the EPR-dependent delivery of IV administered

nanoparticles.[9] We demonstrated that IP injection of the PCX nanoparticles targets the tumors with minimal distribution to normal tissues. In contrast, IV injected nanoparticles mainly distributed to the liver and showed negligible tumor accumulation. Both physicochemical properties of the nanoparticles and biological characteristics of the tumor appear to contribute to the enhanced and EPR-independent delivery of the nanoparticles. First, effective peritoneal retention extended the exposure of the tumors to the high concentration of the nanoparticles. PCX nanoparticles demonstrated good colloidal stability upon protein binding in the ascites, which likely contributed to their widespread distribution in the peritoneal cavity. Meanwhile, the absorption of the nanoparticles into systemic circulation was still inevitable as a result of lymphatic drainage.[49] Second, the nanoparticles accumulated in the tumors due to the specific features of the peritoneal tumors. There is a lack of mesothelium on the surface of the orthotopic tumors and metastases. In contrast, abdominal organs are covered by compact peritoneum that prevents the entry of the nanoparticles.[19] Besides the lack of surface barrier, the higher metabolic activity of the tumors was also reported to promote internalization of the nanoparticles.[52] Third, nanoparticles penetrated deeply into the tumors directly from the tumor periphery to the tumor center in a manner independent of the tumor blood vessels. The small particle size and optimized hydrophobicity of the PCX nanoparticles possibly facilitated tumor penetration of the nanoparticles.[54] The hypovascular structure of PDAC tumors also reduced the clearance of nanoparticles from the tumors, which further likely contributed to the observed accumulation.[55] Previous studies focused on the receptor-mediated targeting for peritoneal tumor imaging or therapy after IP injection.[25,26] Our study reports a more general local delivery strategy that is based on the damaged mesothelial membrane on the tumor surface and is independent of an EPR effect. The IP injection of the PCX nanoparticles provides a mechanism of tumor delivery that is not dependent on the EPR effect and thus may have better potential for successful clinical application. The existence of the EPR effect, especially in human PDAC, has been under intense scrutiny and implicated in the clinical failures of nanomedicines.[56]

Despite multiple promoting factors found, we do not fully understand the mechanism for the unexpectedly high tumor delivery efficacy of the IP-injected PCX nanoparticles. Optimization of the physicochemical properties of the nanoparticles will likely allow improved IP delivery. For example, a large portion of PCX nanoparticles was absorbed into systemic circulation. We aim to improve the bioadhesive properties of the nanoparticles to extend their retention in the peritoneal cavity.[48] There are various types of cells in the peritoneal cavity, which may be involved in the effective tumor penetration of the PCX nanoparticles.[19,57] It is conceivable that the tumor accumulation and penetration is a cell-mediated process, most likely with involvement of peritoneal macrophages. The interactions between nanoparticles and macrophages are complex and likely to determine the delivery efficacy. To understand the interaction is very important for understanding the mechanism of IP delivery and is also our future study direction. Moreover, we intend to further improve the penetration ability of nanoparticles. Through the introduction of a tumor-penetrating peptide, the penetrating depth can be increased further, which will expand the use of nanoparticles for bigger tumors in large animal models and ultimately in humans.[25,58] Quantitative

analysis methods like stem-loop PCR will have to be deployed to fully understand the blood absorption, IP distribution, metabolism, and secretion of the IP-injected nanoparticles.

Inhibition of Tumor Growth and Depletion of Desmoplasia without Increasing Immunosuppression.

Treatment efficacy of the IP-administered nanoparticles was initially tested in the mice bearing the KPC8060 orthotopic pancreatic tumor (Figure 4A). No changes in the body weight during treatment (Figure 4B) confirmed that the PCX nanoparticles caused no gross toxicity in the animals. Codelivery of anti-miR-210 and siKRAS^{G12D} effectively delayed primary tumor growth according to semiquantitative ultrasound imaging analysis (Figure S16). After treatment, primary pancreatic tumors were harvested for analysis. In comparison with the PBS group, treatment with PCX/(anti-miR-NC +siNC) nanoparticles showed a negligible effect on the primary tumor growth, confirming that CXCR4 inhibition by PCX alone has no significant effect on tumor cell proliferation. Both PCX/(anti-miR-210+siNC) and PCX/(anti-miR-NC +siKRAS^{G12D}) inhibited primary tumor growth by ~45%. The combination PCX/(anti-miR-210+siKRAS^{G12D}) nanoparticles showed the best activity with 60% primary tumor growth inhibition (Figure 4C). Successful delivery of the two therapeutic RNAs was confirmed from the levels of miR-210, and KRAS^{G12D} quantified by qRT-PCR and Western blot in the tumors of treated mice. IP treatment with the PCX/(anti-miR-210+siKRAS^{G12D}) resulted in 76% downregulation of miR-210 and 74% silencing of the KRAS^{G12D} expression in the isolated tumors (Figure 4D,E).

K_i-67 immunohistochemical staining of the tumors was performed to study the antiproliferative activity of the nanoparticles (Figure 4F). The PCX/(anti-miR-210+siK-RAS^{G12D}) treatment showed the best antiproliferative activity, with only 26% of K_i-67$^+$ cells. In comparison, silencing of miR-210 or KRAS^{G12D} alone resulted in modest antiproliferative activity. PCX/(anti-miR-210+siKRAS^{G12D}) nanoparticles also induced the greatest necrosis in the tumor based on HE staining (Figure S17A). These results confirm that IP delivery of anti-miR-210 and siKRAS^{G12D} by the PCX nanoparticles effectively silenced both miR-210 and KRAS^{G12D} in the tumor, which resulted in combined activity to inhibit primary tumor growth through a cooperative antiproliferative effect.

Histological analysis of fibrosis markers was performed to study the effect of the PCX nanoparticles on tumor desmoplasia (Figure 4G). Control PCX/(anti-miR-NC +siNC) nanoparticles reduced the activation of PSCs (~21% αSMA$^+$) in comparison with PBS group (~30% αSMA$^+$). Silencing of miR-210 by PCX/(anti-miR-210+siNC) nanoparticles (~11% αSMA$^+$) and PCX/(anti-miR-210+siK-RAS^{G12D}) nanoparticles (~9% αSMA$^+$) further significantly inhibited the activation of PSCs. Silencing of siKRAS^{G12D} had no additional effect on the activation status of PSCs in the tumors (~20% αSMA$^+$).

Activated PSCs produce collagen which is the main component of ECM in PDAC. The combined PCX nanoparticles decreased collagen content in the tumors to ~9% (Figure 4G). PCX/(anti-miR-NC+siNC) nanoparticles (~16% collagen content) and miR-210 downregulation (~9% collagen content) also significantly decreased collagen in tumor compared with PBS (~24% collagen). This result is consistent with the inhibition of activated PSCs and confirms that PCX/(anti-miR-210+siKRAS^{G12D}) nanoparticles

cooperatively reduced activation of PSCs and extent of tumor fibrosis through combined CXCR4 blockade and miR-210 silencing. Activated PSCs are also a driver of angiogenesis.[27,59] PCX/(anti-miR-210+siKRAS^{G12D}) nanoparticles presented significant antiangiogenic activity as indicated by reduced CD31^{+} blood vessel density in the tumors (Figure S17B). These results demonstrated that our nanoparticles have a combined ability to decrease desmoplasia in PDAC through silencing of miR-210 and inhibition of CXCR4 signaling and to decrease angiogenesis due to depletion of activated PSCs.[27]

Tumor stroma contributes to the establishment of an immunosuppressive tumor microenvironment in PDAC. Modulation of tumor stroma represents a therapeutic approach to augment immunotherapy.[60] The effect of depletion of tumor stroma on cancer immune response remains controversial with both pro- and antitumorigenic roles identified. It has even been reported that depletion of PSCs in the PDAC stroma enhanced immunosuppression and promoted tumor progression through facilitating infiltration of suppressive immune cells.[6] Considering the risk of stromal depletion on the immune response, we analyzed the effect of the nanoparticle treatment on the tumor immune microenvironment. Dense desmoplasia is a physical barrier to the infiltration of cytotoxic T lymphocytes. As shown in Figure 4H, treatment with CXCR4-inhibiting PCX/(anti-miR-NC +siNC) nanoparticles increased CD8^{+} T cells infiltration. Interestingly, downregulation of miR-210 in the tumors further enhanced infiltration of CD8^{+} T cells. These results confirmed a combined effect of PCX/(anti-miR-210+siKRAS^{G12D}) nanoparticles on tumor-accumulation of CD8^{+} T cells. A recent study confirmed that reduction of desmoplasia by CXCR4 blockade does indeed increase the tumoral infiltration of T cells.[61] Silencing of miR-210 increased CD8^{+} T cells in the tumor possibly through regulation of T cell differentiation.[62] Moreover, significantly decreased levels of suppressive M2 tumor-associated macrophages (CD206^{+} M2 TAMs) were also observed in the tumors after nanoparticle treatment (Figure 4H). Inhibition of the CXCR4/CXCL12 axis by PCX was believed to contribute to the inhibition of M2 polarization of TAMs.[63,64] This result demonstrated the effect of the PCX nanoparticles on modulation of TAMs to reverse immunosuppressive tumor microenvironment. We also determined the levels of intratumoral cytokines to study the effect of nanoparticles on the tumor immunosuppressive microenvironment. Pro-inflammatory cytokines IFN-γ and TNF-α are mainly secreted by cytotoxic T-cells and are involved in T-cell killing for tumor suppression.[65] Treatment with nanoparticles significantly increased the secretion of IFN-γ and TNF-α (Figure S17C), which further confirmed the immunostimulatory effect of the PCX nanoparticles.

Depletion of desmoplasia potentially induces cancer stem cell-like phenotype, which possibly enhances tumorigenicity and decreases survival.[6,66] Here, we compared the stemness of the tumors after nanoparticle treatment with immunofluorescence analysis of cancer stem cell markers aldehyde dehydrogenase 1-A1 (ALDH1A1) and CD44.[67] The treatment with PCX nanoparticles did not increase the ALDH1A1^{+} and CD44^{+} cell populations in the tumors. In fact, we have observed statistically significant decreases in the different treatment groups. This result indicates that the treatment with the triple nanotherapy did not increase cancer stemness in the tumors.

Inhibition of Metastasis and Improvement of Survival.

Metastasis is widely seen in PDAC patients and is a main cause of cancer-related deaths.[68] After establishing promising efficacy of the PCX nanoparticles on the inhibition of the primary tumor growth and modulation of the tumor microenvironment, we set to investigate the antimetastatic activity of the particles. The used PDAC tumor model is highly metastatic as evidenced by local invasion and widespread metastases found in the untreated animals (group G1). We observed macroscopic metastases in the liver, spleen, kidney, intestine, stomach, abdominal wall, and diaphragm. Treatment with the CXCR4-inhibiting PCX/(anti-miR-NC+siNC) nanoparticles showed clear antimetastatic activity, indicated by the reduced metastatic frequencies in the broad range of examined tissues when compared with the G1 group (Figure 5A). The delivery of anti-miR-210 and siKRAS^{G12D} further improved the antimetastatic activity of the PCX nanoparticles, with PCX/(anti-miR-210+siKRAS^{G12D}) completely inhibiting the metastasis to all observed tissues except pancreas-adjacent splenic invasion. Importantly, the PCX/(anti-miR-210+siKRAS^{G12D}) nanoparticles completely inhibited liver metastasis, which is the major metastatic site in PDAC patients (Figure 5B and Figure S18). Nanoparticle treatment started at a late tumor stage (2 weeks) when the local splenic invasion occurred. This led to the failure of nanoparticles to inhibit splenic invasion. HE staining showed a decrease in the metastasis area in tissues of animals treated with the PCX nanoparticles (Figure 5C). These results confirmed the combined antimetastatic activity of PCX/(anti-miR-210+siKRAS^{G12D}) nanoparticles through inhibition of CXCR4 and silencing of miR-210 and KRAS^{G12D}.

PCX/(anti-miR-210+siKRAS^{G12D}) nanoparticles inhibited primary tumor growth, modulated stromal microenvironment, and inhibited widespread metastasis. We thus next studied the effect of nanoparticle treatment on survival in the orthotopic PDAC model. In comparison with the PBS group, even the CXCR4 inhibition alone with the PCX/(anti-miR-NC+siNC) treatment significantly increased median survival by 19%. PCX/(anti-miR-210+siNC) and PCX/(anti-miR-NC+siK-RAS^{G12D}) further prolonged the animal survival by 31% and 34%, respectively. PCX/(siKRAS+miR-210) nanoparticles achieved a cooperative activity to improve survival by 50% (Figure 5D).

Toxicity evaluation of the IP-injected nanoparticles was performed. No obvious tissue damage was found in comparison with the PBS group according to HE staining of major organs (Figure S19). Blood was collected from mice on day 28 for whole blood analysis and blood biochemistry. PCX/(anti-miR-NC+siKRAS^{G12D}) nanoparticles treatment did not alter white blood cell, lymphocyte, monocyte, neutrophil, or red blood cell count when compared with the PBS group, which suggested no adverse hematologic effects, such as hemolytic anemia caused by the nanoparticles (Table S1). Liver enzymes and renal function biomarkers were also measured. The concentrations of AST, ALT, BUN, and creatinine were within the normal range (Table S2). These results confirmed the overall safety of IP injected PCX nanoparticles.

Overall, our approach demonstrated the benefits of the triple combination therapy strategy in comparison with individual nucleic acid drug therapies. Despite the confirmed improved antitumor activity both *in vitro* and *in vivo*, the detailed analysis of signaling pathways involved in these combined therapeutics need to be studied in advanced culture models of

pancreatic cancer cells/PSCs. Our approach will also benefit from combining with conventional chemotherapy and immunotherapy such as T cell checkpoint antagonists[61,69] due to the reduced delivery barrier of stromal desmoplasia and stimulated immune microenvironment after nanoparticle treatment.

No anticancer treatment has been approved by the U.S. Food and Drug Administration specifically for IP administration, but multiple clinical studies of IP injected therapeutics are carried out to treat patients with peritoneal cancers. The results demonstrate the potential of IP delivery to improve treatment efficacy and to lower systemic toxicity.[19,70,71] There are currently several methods of regional IP delivery used in the treatment of human cancers, the most common of them being hyperthermic intraperitoneal chemotherapy.[19] While the current methods use only traditional chemotherapeutics, there is a growing realization that IP delivery of other types of therapies, such as the one described here, may bring advantages not seen with systemic delivery.[72,73]

CONCLUSION

This study demonstrates the benefits of EPR-independent delivery of nanomedicine by IP administration for PDAC therapy and provides an alternative to conventionally used EPR-dependent delivery by IV injection. Triple-targeting of cancer cells, stroma, and their interactions by nanotherapy represents a safe and effective approach for combination PDAC therapy.

MATERIALS AND METHODS

Materials.

Dulbecco's phosphate buffered saline (PBS), Dulbecco's modified Eagle medium (DMEM), fetal bovine serum (FBS), trypsin, penicillin, and streptomycin were purchased from Thermo Scientific (Waltham, MA). miR-210–3p-Hairpin Inhibitor (anti-miR-210, mature miRNA sequence: CUGUGCGUGUGACAGCGGCUGA), negative control miRNA inhibitor (anti-miR-NC, mature miRNA sequence: UCACAACCUCCUAGAAAGAGUAGA), siRNA targeting $KRAS^{G12D}$ ($siKRAS^{G12D}$, sense sequence, 5′-GUUGGAGCUGAUGGCGUAGdTdT-3′), negative control siRNA (siNC, sense sequence, 5′-UCACAACCUCCUAGAAAGAGUAGA-3′), and carboxyfluorescein (FAM) labeled siRNA (FAM-siRNA) were from Dharmacon (Lafayette, CO). Average M_w of anti-miRNA is 18 500 g/mol. Average M_w of siRNA is 13 300 g/mol. AMD3100 was provided by Biochempartner (Shanghai). Real-time (RT)-PCR primers were from Invitrogen (Carlsbad, CA). Other reagents were provided by Fisher Scientific and used as received unless stated otherwise.

Synthesis and Characterization of Polymer.

PCX was synthesized and characterized as previously described.[43,45] Michael polyaddition of AMD3100 and HMBA resulted in the polymeric AMD3100. The equal molar ratio of HMBA (1 mmol) and AMD3100 (1 mmol) were dissolved in 9 mL of methanol/water (7:3 v/v) mixture. The glass vial with the reactants was purged with nitrogen and the reaction was carried out at 37 °C for 3 days in the dark. Then an additional 0.1 mmol of AMD3100 was

added to consume the residual acrylamide groups. The reaction mixture was dialyzed against methanol (3500 MWCO) for 1 day. Then methanol was evaporated, and polymeric AMD3100 was further dried in vacuum. The overall yield is around 91%. The structure of polymeric AMD3100 was confirmed by ^{1}H NMR using Varian INOVA (500 MHz). The molecular weight was determined by gel permeation chromatography (GPC) using Agilent 1260 Infinity LC system with a miniDAWN TREOS multiangle light scattering detector and an Optilab T-rEX refractive index detector (Wyatt Technology, Santa Barbara, CA). TSKgel G3000PW$_{XL}$-CP column (Tosoh Bioscience LLC, PA) was used at a flow rate of 0.5 mL min^{-1} (sodium acetate buffer, pH 5). Astra 6.1 software was used to analyze results.

Cholesterol was conjugated to polymeric AMD3100 by reaction with cholesteryl chloroformate. Polymeric AMD3100 (650 mg) and DIPEA (346.6 mg, 2.68 mmol) were dissolved in anhydrous methylene chloride. Cholesteryl chloroformate (140.5 mg, 0.31 mmol) was dissolved in anhydrous methylene chloride and added dropwise into the polymeric AMD3100 solution in ice-bath. The reaction was carried out overnight, and the product was purified by dialysis against methanol (3500 MWCO) for 1 day, followed by dialysis against HCl solution (pH = 4) for 1 day and deionized water for another day. The final PCX product was obtained as a hydrochloride salt through lyophilization. The yield of PCX is around 78%. The structure of PCX and the amount of conjugated cholesterol were characterized by ^{1}H NMR on Varian INOVA (500 MHz). Succinimidyl ester of Alexa Fluor 647 carboxylic acid (Life Technologies, OR) was conjugated to PCX to obtain AlexaFluor 647 labeled PCX (AF647-PCX) following the manufacturer's protocol.

Cell Culture.

Primary tumor cell line KPC8060 derived from KPC PDAC mouse model (Kras$^{LSL-G12D/+}$; Trp53$^{LSL-R172H/+}$; Pdx-1-Cre) was provided by Dr. Hollingsworth at UNMC. The human cell line of metastatic pancreatic cancer COLO357 was kindly provided by Dr. Batra at UNMC. Both cell lines were cultured in high-glucose DMEM with 10% FBS, penicillin (100 U/mL), streptomycin (100 μg/mL) at 37 °C with 5% CO_2 in a humidified chamber. Human pancreatic stellate cells (Catalog #: 3830) were purchased from ScienCell Research Laboratories (CA, USA) and cultured in Stellate Cell Medium (SteCM, Cat. #5301) at 37 °C with 5% CO_2 in a humidified chamber.

CXCR4 Antagonism Assay.

CXCR4 redistribution assay was employed to determine the CXCR4 antagonism efficacy of compounds. U2OS cells with the EGFP-CXCR4 fusion protein (Fisher Scientific) were cultured in DMEM with 2 mM L-glutamine, 10% FBS, 1% Pen–Strep, and 0.5 mg/mL G418. Cells were seeded in black 96-well microplates 24 h before treatment. Cells were washed with assay buffer before treatment and then treated with tested compounds for 30 min. CXCL12 was added for another 1 h incubation. Cells were fixed and stained with Hoechst 33258. Quantification of the internalization of the CXCR4 receptors was performed with Cellomics ArrayScan V High Content Analysis Reader (Thermo Scientific) and SpotDetectorV3 BioApplication software. Dose–response curves were obtained based on % CXCR4 internalization calculated relative to the AMD3100 group (100%) and CXCL12

only group (0%). EC50 value (concentration inducing 50% CXCR4 antagonism) of tested compounds was calculated with Prism GraphPad software.

Cytotoxicity.

Cytotoxicity of PCX was tested by CellTiter-Blue Cell Viability Assay. Cells were treated with 100 μL of polymer solutions with various concentrations in culture medium for 24 h. The medium was then replaced by a mixture of 100 μL of media and 20 μL of CellTiter-Blue reagent. The fluorescence [F] (Ex = 560 nm, Em = 590 nm) was measured using Microplate Reader (Molecular Devices, CA) after 2 h incubation. The relative cell viability (%) was expressed as [F]sample/[F]untreated × 100. The IC50 values (50% cell growth inhibition) were obtained from a dose–response analysis in GraphPad Prism.

Analysis of CXCR4 Expression on Cell Surface.

Cells were incubated with allophycocyanin (APC) labeled CXCR4 antibody (BD Biosciences, CA) for 1 h at 4 °C. The isotype-matched antibody was employed to assess the background fluorescence. Cells were subjected to a FACS Calibur (BD Bioscience, Bedford, MA) and results were analyzed by FlowJo software (Tree Star Inc., OR).

Transwell Migration Assay.

Cells were trypsinized, washed with PBS, and resuspended in medium without serum. Cells pretreated with tested compounds for 15 min or without treatment were added in the cell culture inserts (8.0 μm pores, BD Biosciences) in 300 μL of serum-free medium (3×10^5 cells per insert). The lower transwell chamber was filled with 600 μL of serum-free medium containing 20 nM CXCL12. After 20 h incubation, removal of cells in the top chamber was done using cotton swabs. Migrated cells were fixed, stained with 0.2% Crystal Violet, and observed under an EVOS xl microscope. The results were calculated as the percentage of migrated cells relative to PBS-treated cells/imaging field ± SD ($n = 3$).

Preparation and Characterization of Nanoparticles.

PCX/(anti-miR+siRNA) nanoparticles were prepared by mixing a predetermined volume of PCX with an anti-miR and siRNA equal molar solution (20 μM in pH 7.4 HEPES) and vortexing for 10 s. Agarose gel electrophoresis was performed to test the ability of PCX to condense anti-miR and siRNA. Nanoparticles at various polycation-to-(anti-miR+siRNA) weight ratios were loaded in the gel (0.5 μg/mL ethidium bromide) and ran in 0.5 × Tris/Borate/EDTA buffer for 15 min (100 V). The gels were observed with KODAK Gel Logic 100 imaging system. Dynamic light scattering (DLS) was used to measure the hydrodynamic diameter and zeta potential of the nanoparticles using ZEN3600 Zetasizer Nano-ZS (Malvern Instruments Ltd., Massachusetts, USA). Nanoparticle morphology was visualized using TEM (Tecnai G2 Spirit, FEI Company, USA) with NanoVan negative staining (Nanoprobes, USA) and MultiMode AFM NanoScope IV system (Bruker Instruments, Santa Barbara, CA) operating in tapping mode. Heparin displacement assay was applied to analyze anti-miR and siRNA release from nanoparticles. Nanoparticles (w/w = 2) were incubated with heparin solution for 30 min, then assayed by gel electrophoresis. For the enzyme stability test, free anti-miR+siRNA solution and nanoparticles were

incubated with FBS (50% v/v) or RNase I (2 U/μL) at 37 °C, respectively. The samples were collected at predetermined time points, treated with heparin, and analyzed by gel electrophoresis.

Cellular Uptake and Intracellular Trafficking.

Cells were seeded in 12-well plates 24 h before treatment. Cells were treated by nanoparticles prepared with AF647-PCX and FAM-siRNA (w/w = 2, 100 nM FAM-siRNA) for 4 h in the presence of FBS. Cells were washed by PBS, detached with trypsin and analyzed on a FACS Calibur (BD Bioscience, Bedford, MA). Subcellular distribution of nanoparticles was observed by confocal microscopy. Cells were seeded on a 20 mm glass-bottom culture dish (Nest) 24 h before treatment. AF647-PCX/FAM-siRNA nanoparticles were added and incubated for 4 h. Cells were washed, stained with Hoechst 33258, and visualized under an LSM 800 Laser Scanning Microscope (Zeiss, Jena, Germany). To observe the endo/lysosomal release, cells were treated by nanoparticles for 2 or 6 h. Then cells were stained with LysoTracker Red DND-99 (Life Technology, USA) and visualized with a confocal microscope.

Tumor Penetration in Multicellular Tumor Spheroids.

KPC8060 cells were seeded in ultralow attachment 24-well plates (Corning, New York) at a density of 5×10^4 cells per well. The spheroid diameter reached about 300 μm after culturing for 10 days. AF647-PCX/FAM-siRNA nanoparticles were incubated with spheroids for 12 h. Spheroids were washed with PBS, fixed with 4% paraformaldehyde and observed with a confocal microscope (z-stack with 10 μm intervals). Fluorescence images were transformed to surface plots by ImageJ software. The spheroids were also trypsinized to single-cell suspension for flow cytometry analysis.

Quantitative Real-Time Polymerase Chain Reaction (qRT-PCR).

Cancer cells were incubated with PCX nanoparticles (anti-miR 50 nM, siRNA 50 nM) for 48 h in the presence of FBS. Total RNA was extracted from cultured cells using the mirVana miRNA Isolation Kit (Ambion, USA). MiRNA level was measured by TaqMan qRT-PCR. RNA (10 ng) was converted to cDNA by TaqMan miRNA reverse transcription kit (Applied Biosystems) and primers for miR-210 or Z30 (internal control) (Applied Biosystems, CA). PCR reaction was conducted on Rotor-Gene Q (QIAGEN) using TaqMan Universal Master Mix and primers for miR-210 or Z30 (Applied Biosystems). Expression of $KRAS^{G12D}$ was quantified using SYBR Green RT-PCR. RNA (0.5 μg) was reverse-transcribed to cDNA with QuantiTect reverse transcription kit (Qiagen). PCR reaction was performed on Rotor-Gene Q (QIAGEN) using the QuantiFast SYBR Green PCR kit (Qiagen). The GAPDH primer assay (QIAGEN) was used following the manufacturer's protocol. $KRAS^{G12D}$ primer (forward 5′-CGCAGACTTACTTCCCCGGC; reverse, 5′-CGCTCAATTCCTCAACCACG) was used. Relative miRNA or mRNA levels were calculated according to the comparative threshold value (Ct) method. Human PSCs were also treated with nanoparticles in serum free medium for 48 h. Then total RNA was extracted for analysis of miR-210 level in cells using qRT-PCR assay described above.

Apoptosis Assay by DAPI Staining.

Cells were treated with nanoparticles (50 nM anti-miR, 50 nM siRNA) for 48 h. Cells were stained with 2 μg/mL of DAPI (4′, 6-diamidino-2′-phenylindole dihydrochloride) and observed under EVOS xl fluorescence microscope (Thermo, US). Apoptotic nuclei (condensed and fragmented morphology) were counted and presented as a percentage of total nuclei per observation field.

Cell Killing Assay.

Cytotoxicity of the nanoparticles was evaluated by CellTiter-Blue assay. Cells were treated with nanoparticles (50 nM anti-miR, 50 nM siRNA) for 48 h. The medium was then replaced by a mixture of 100 μL of media and 20 μL of CellTiter-Blue reagent. After 2 h of incubation, fluorescence [F] (Ex = 560 nm, Em = 590 nm) was measured using Microplate Reader (Molecular Devices, CA). The relative cell viability (%) was expressed as [F]sample/[F]untreated × 100.

Colony Formation Assay.

Cells were treated with nanoparticles (50 nM anti-miR, 50 nM siRNA) for 4 h. Cells were seeded to 12-well plates (KPC8060 cells 200/well, COLO357 cells 600/well). After growth for 12 days, cells were fixed, stained with Crystal Violet (0.2%), washed with water, and photographed. Colony number in each well was counted.

Immunofluorescence of Stromal Markers in PSCs.

Human PSCs were seeded in eight-well chambered cover glass (Thermo Fisher) and treated with nanoparticles in serum free medium for 48 h. After that, cells were fixed in 4% paraformaldehyde for 15 min, permeabilized in 0.2% Triton X-100 for 1 h, and blocked with 5% bovine serum for 30 min. αSMA or Collagen I primary antibodies in 1% BSA were diluted and incubated with cells at 4 °C overnight, respectively. Cells were washed several times with PBS after the primary antibody incubation and changed with antirabbit IgG Alexa Fluor 488 secondary antibody (Thermo Fisher) for 1 h. The nuclei were counterstained with Hoechst 33342 for 15 min. Images were acquired using the Zeiss LSM 800 confocal microscope.

Orthotopic Pancreatic Cancer Model.

Animal experiment protocols have been approved by the University of Nebraska Medical Center Institutional Animal Care and Use Committee. Orthotopic KPC-derived pancreatic cancer model was established by injection of KPC8060 cells into the pancreas. Briefly, KPC8060 cells were trypsinized and resuspended in 1:1 mixture of PBS/Matrigel. Female C57BL/6 mice (6 weeks old) from Charles River Laboratories were anesthetized by IP injection of ketamine/xylazine solution. An incision (~1 cm) was made in the peritoneum at the midabdomen region below the sternum. For this, 2.5×10^4 of KPC8060 cells (40 μL) were injected into the tail of the pancreas. The abdomen was closed with a two-layer suture with 5–0 chromic catgut and soft staple. The staples were removed 7 days after surgery.

Blood Circulation Time.

Orthotopic pancreatic tumor-bearing mice (3 weeks after tumor implantation, tumor diameter ~10 mm) were IV or IP administrated with 200 μL of AF647-PCX/FAM-siRNA nanoparticles (5 mg/kg AF647-PCX, 2.5 mg/kg FAM-siRNA). At 2 min, 0.25, 1, 4, and 24 h post injection, about 100 μL of blood from the retro-orbital venous plexus of each mouse was collected in heparin-treated tubes and imaged with Xenogen IVIS 200 (Ex = 640 nm, Em = 680 nm), which was followed by fluorescence analysis by the instrument software.

Biodistribution.

Orthotopic pancreatic tumor-bearing mice (tumor diameter ~10 mm) were IV or IP injected with 200 μL of AF647-PCX/FAM-siRNA nanoparticles (5 mg/kg AF647-PCX, 2.5 mg/kg FAM-siRNA). At 4 and 24 h post injection, mice were sacrificed and imaged using Xenogen IVIS 200 (Ex = 640 nm, Em = 680 nm). Tumors and major organs were also harvested for *ex vivo* fluorescence imaging. For CXCR4 receptor competition assay, anti-CXCR4 antibody (UMB2, Abcam) was IP injected into mice (100 μg/mouse) 30 min before nanoparticles administration. The instrument software was used to analyze the fluorescence signal from each tumor or organ. Tumors were embedded in an OCT compound, cut into 10 μm frozen sections, stained with CD31 antibody (Cy3), and observed using a confocal microscope. Moreover, tumors were also stained with αSMA antibody (Cy3) to label PSCs and visualized under a confocal microscope. Moreover, we performed HE staining to study the mesothelium of tissues and tumors of the orthotopic KPC model. We also analyzed mesothelium in KPC mice with spontaneously developed tumors and in samples from human PDAC patients. Section slides from the wild-type (WT) KPC mice were provided by Dr. Hollingsworth at UNMC. The WT KPC mice carry the PDX-1-Cre transgene, the *LSL-KRAS*^{G12D} knock-in mutation, and the *LSL-Trp53*^{R172H} knock-in mutation. Sections were collected from WT KPC mice at age of 19–21 weeks at which stage the animals develop primary pancreatic tumor and peritoneal metastasis. The section slides of healthy human pancreas and liver tissues, and PDAC patient primary pancreatic tumor and liver metastases were obtained from the UNMC Rapid Autopsy Program with informed consent from all patients and approval from Institutional Review Board.

Antitumor Activity *in vivo*.

Mice were randomly assigned to five groups ($n = 5$) and IP injected with PBS, PCX/(anti-miR-NC+siNC), PCX/(anti-miR-210+siNC), PCX/(anti-miR-NC+siKRAS^{G12D}), and PCX/(anti-miR-210+siKRAS^{G12D}), respectively. PCX/(anti-miRNA +siRNA) nanoparticles (5 mg/kg PCX) were injected at days 14, 16, 18, 20, 22, 24, and 26 post tumor-implantation. Mouse body weight was recorded during treatment. Tumor growth was monitored using a Vevo 3100 ultrasound system (Fujifilm, VisualSonics, Toronto, ON) with an MX550D transducer (40 MHz center frequency, 40 μM axial resolution) in B-mode. Briefly, mice were anesthetized using isoflurane and placed on a stationary, heated platform equipped with a motorized transducer adapter to acquire 3D images. Vevo Lab software was used to reconstruct tumor shapes and assess tumor volumes. On days 28, blood was harvested from retro-orbital venous plexus of the mouse for whole blood analysis and serum biochemistry test. Mice were sacrificed, and primary tumor weight and metastatic sites were evaluated in

each experimental group. Total RNA in the tumor was isolated using mirVana miRNA Isolation Kit. Protein was also harvested from tumor tissues by RIPA Lysis buffer. Tumors and major organs were fixed in 4% paraformaldehyde and sectioned for histochemical analysis. Survival analysis was performed on mice with the same treatment method but using nine mice per group.

Western Blot.

Protein concentration was measured by BCA kit (Promega, USA). The protein solution was denatured, loaded to 10% SDS-PAGE electrophoresis gel (running 2 h at 120 V), and transferred to a nitrocellulose membrane (running 1 h at 300 mA). The membrane was blocked, incubated with primary antibody overnight at 4 °C, washed, and incubated with IgG HRP-linked antibody (Cell Signaling Technology, USA). Finally, membranes were visualized using Pierce ECL Western Blotting Substrate (Thermo Scientific, USA). Western blot bands were quantified with ImageJ software.

Histochemical Analysis.

Tumor or organ sections were analyzed with HE and Masson's trichrome staining (collagen coverage percentage in each observation field was quantified by ImageJ software). Antigen retrieval was conducted. K_i-67 immunohistochemical staining was performed to study the proliferation of tumor cells. For immunofluorescence staining, tumor slides were treated with endogenous peroxidase inhibitor, incubated with primary antibody at 37 °C for 32 min, incubated with horseradish peroxidase (HRP)-conjugated secondary antibody at 37 °C for 32 min, and incubated with Discovery FITC Kit (Roche). Sections were also counterstained with DAPI for nucleus visualization. Immunohistochemistry images were taken on the EVOS xl microscope (Thermo, US). Immunofluorescence slides were mounted with antifade reagent and observed using a confocal microscope (LSM 800).

Blood Chemistry Analysis.

Blood was withdrawn in heparin tubes and analyzed using Vetscan VS (Abaxis). Creatinine, urea (BUN), alanine transaminase (ALT), and aspartate transaminase (AST) were measured by assay kit (Bioassay Systems, CA, USA) according to the protocol.

Statistical Analysis.

Results are presented as mean ± SD. ANOVA was used to analyze differences among multiple groups followed by Tukey's multiple comparison test. Student's t test was used to analyze the statistical significance between the two groups. $P < 0.05$ was considered as a minimal level of significance. All statistical analysis was performed with GraphPad Prism v5.

Supplementary Material

Refer to Web version on PubMed Central for supplementary material.

ACKNOWLEDGMENTS

This work was supported by start-up funds from the University of Nebraska Medical Center, National Institutes of Health (R41TR001312), and the Nebraska Department of Economic Development (16-01-298). Fellowship from China Scholarship Council for Y.X. and Y.H. is gratefully acknowledged. We thank Dr. Solheim for the feedback on the manuscript, Dr. Hollingsworth for providing tissue samples from spontaneous KPC mouse PDAC, and Dr. Grandgenett for sharing tissue samples from pancreatic cancer patients from the Rapid Autopsy Program at UNMC.

REFERENCES

(1). Siegel RL; Miller KD; Jemal A Cancer Statistics, 2017. Ca-Cancer J. Clin 2017, 67, 7–30. [PubMed: 28055103]

(2). Rahib L; Smith BD; Aizenberg R; Rosenzweig AB; Fleshman JM; Matrisian LM Projecting Cancer Incidence and Deaths to 2030: The Unexpected Burden of Thyroid, Liver, and Pancreas Cancers in the United States. Cancer Res. 2014, 74, 2913–2921. [PubMed: 24840647]

(3). Conroy T; Desseigne F; Ychou M; Bouché O; Guimbaud R; Bécouarn Y; Adenis A; Raoul J-L; Gourgou-Bourgade S; de la Fouchardière C; et al. FOLFIRINOX *Versus* Gemcitabine for Metastatic Pancreatic Cancer. N. Engl. J. Med 2011, 364, 1817–1825. [PubMed: 21561347]

(4). Erkan M; Hausmann S; Michalski CW; Fingerle AA; Dobritz M; Kleeff J; Friess H The Role of Stroma in Pancreatic Cancer: Diagnostic and Therapeutic Implications. Nat. Rev. Gastroenterol. Hepatol 2012, 9, 454–467. [PubMed: 22710569]

(5). Neesse A; Algül H; Tuveson DA; Gress TM Stromal Biology and Therapy in Pancreatic Cancer: A Changing Paradigm. Gut 2015, 64, 1476–1484. [PubMed: 25994217]

(6). Ozdemir BC; Pentcheva-Hoang T; Carstens JL; Zheng X; Wu CC; Simpson TR; Laklai H; Sugimoto H; Kahlert C; Novitskiy SV; et al. Depletion of Carcinoma-Associated Fibroblasts and Fibrosis Induces Immunosuppression and Accelerates Pancreas Cancer with Reduced Survival. Cancer Cell 2014, 25, 719–734. [PubMed: 24856586]

(7). Olive KP; Jacobetz MA; Davidson CJ; Gopinathan A; McIntyre D; Honess D; Madhu B; Goldgraben MA; Caldwell ME; Allard D; et al. Inhibition of Hedgehog Signaling Enhances Delivery of Chemotherapy in A Mouse Model of Pancreatic Cancer. Science 2009, 324, 1457–1461. [PubMed: 19460966]

(8). Han X; Li Y; Xu Y; Zhao X; Zhang Y; Yang X; Wang Y; Zhao R; Anderson GJ; Zhao Y; et al. Reversal of Pancreatic Desmoplasia by Re-Educating Stellate Cells with A Tumour Microenvironment-Activated Nanosystem. Nat. Commun 2018, 9, 3390. [PubMed: 30139933]

(9). Provenzano PP; Cuevas C; Chang AE; Goel VK; Von Hoff DD; Hingorani SR Enzymatic Targeting of the Stroma Ablates Physical Barriers to Treatment of Pancreatic Ductal Adenocarcinoma. Cancer Cell 2012, 21, 418–429. [PubMed: 22439937]

(10). Rhim AD; Oberstein PE; Thomas DH; Mirek ET; Palermo CF; Sastra SA; Dekleva EN; Saunders T; Becerra CP; Tattersall IW; et al. Stromal Elements Act to Restrain, Rather Than Support, Pancreatic Ductal Adenocarcinoma. Cancer Cell 2014, 25, 735–747. [PubMed: 24856585]

(11). Catenacci DV; Junttila MR; Karrison T; Bahary N; Horiba MN; Nattam SR; Marsh R; Wallace J; Kozloff M; Rajdev L; et al. Randomized Phase Ib/II Study of Gemcitabine Plus Placebo or Vismodegib, A Hedgehog Pathway Inhibitor, in Patients with Metastatic Pancreatic Cancer. J. Clin. Oncol 2015, 33, 4284–4292. [PubMed: 26527777]

(12). Fang J; Nakamura H; Maeda H The EPR Effect: Unique Features of Tumor Blood Vessels for Drug Delivery, Factors Involved, and Limitations and Augmentation of the Effect. Adv. Drug Delivery Rev 2011, 63, 136–151.

(13). Feig C; Gopinathan A; Neesse A; Chan DS; Cook N; Tuveson DA The Pancreas Cancer Microenvironment. Clin. Cancer Res 2012, 18, 4266–4276. [PubMed: 22896693]

(14). Shi J; Kantoff PW; Wooster R; Farokhzad OC Cancer Nanomedicine: Progress, Challenges and Opportunities. Nat. Rev. Cancer 2017, 17, 20–37. [PubMed: 27834398]

(15). Watanabe S; Hayashi K; Toh K; Kim HJ; Liu X; Chaya H; Fukushima S; Katsushima K; Kondo Y; Uchida S; et al. *In vivo* Rendezvous of Small Nucleic Acid Drugs with Charge-Matched Block Catiomers to Target Cancers. Nat. Commun 2019, 10, 1894. [PubMed: 31019193]

(16). Cabral H; Matsumoto Y; Mizuno K; Chen Q; Murakami M; Kimura M; Terada Y; Kano MR; Miyazono K; Uesaka M; et al. Accumulation of Sub-100 nm Polymeric Micelles in Poorly Permeable Tumours Depends on Size. Nat. Nanotechnol 2011, 6, 815–823. [PubMed: 22020122]

(17). Park J; Kadasala NR; Abouelmagd SA; Castanares MA; Collins DS; Wei A; Yeo Y Polymer–Iron Oxide Composite Nanoparticles for EPR-Independent Drug Delivery. Biomaterials 2016, 101, 285–295. [PubMed: 27310916]

(18). Lu Z; Wang J; Wientjes MG; Au JL Intraperitoneal Therapy for Peritoneal Cancer. Future Oncol. 2010, 6, 1625–1641. [PubMed: 21062160]

(19). Dakwar GR; Shariati M; Willaert W; Ceelen W; De Smedt SC; Remaut K Nanomedicine-Based Intraperitoneal Therapy for the Treatment of Peritoneal Carcinomatosis—Mission Possible? Adv. Drug Delivery Rev. 2017, 108, 13–24.

(20). Flessner MF The Transport Barrier in Intraperitoneal Therapy. Am. J. Physiol. Renal. Physiol 2005, 288, F433–F442. [PubMed: 15692055]

(21). Sodek KL; Murphy KJ; Brown TJ; Ringuette MJ Cell–Cell and Cell–Matrix Dynamics in Intraperitoneal Cancer Metastasis. Cancer Metastasis Rev. 2012, 31, 397–414. [PubMed: 22527451]

(22). Deng G; Qu J; Zhang Y; Che X; Cheng Y; Fan Y; Zhang S; Na D; Liu Y; Qu X Gastric Cancer-Derived Exosomes Promote Peritoneal Metastasis by Destroying the Mesothelial Barrier. FEBS Lett. 2017, 591, 2167–2179. [PubMed: 28643334]

(23). Aoki K; Furuhata S; Hatanaka K; Maeda M; Remy J; Behr J; Terada M; Yoshida T Polyethylenimine-Mediated Gene Transfer into Pancreatic Tumor Dissemination in the Murine Peritoneal Cavity. Gene Ther. 2001, 8, 508–514. [PubMed: 11319617]

(24). Colby AH; Berry SM; Moran AM; Pasion KA; Liu R; Colson YL; Ruiz-Opazo N; Grinstaff MW; Herrera VL Highly Specific and Sensitive Fluorescent Nanoprobes for Image-Guided Resection of Sub-Millimeter Peritoneal Tumors. ACS Nano 2017, 11, 1466–1477. [PubMed: 28099801]

(25). Gao N; Bozeman EN; Qian W; Wang L; Chen H; Lipowska M; Staley CA; Wang YA; Mao H; Yang L Tumor Penetrating Theranostic Nanoparticles for Enhancement of Targeted and Image-Guided Drug Delivery into Peritoneal Tumors Following Intraperitoneal Delivery. Theranostics 2017, 7, 1689–1704. [PubMed: 28529645]

(26). Zhao L; Yuan W; Li J; Yang L; Su Y; Peng J; Chen R; Tham HP; Chen H; Lim WQ; et al. Independent of EPR Effect: A Smart Delivery Nanosystem for Tracking and Treatment of Nonvascularized Intra-Abdominal Metastases. Adv. Funct. Mater 2018, 28, 1806162.

(27). Masamune A; Kikuta K; Watanabe T; Satoh K; Hirota M; Shimosegawa T Hypoxia Stimulates Pancreatic Stellate Cells to Induce Fibrosis and Angiogenesis in Pancreatic Cancer. Am. J. Physiol. Gastrointest. Liver. Physiol 2008, 295, 709–717.

(28). Spivak-Kroizman TR; Hostetter G; Posner R; Aziz M; Hu C; Demeure MJ; Von Hoff D; Hingorani S; Palculict TB; Izzo J; et al. Hypoxia Triggers Hedgehog-Mediated Tumor Stromal Interactions in Pancreatic Cancer. Cancer Res. 2013, 73, 3235–3247. [PubMed: 23633488]

(29). Kuninty PR; Bojmar L; Tjomsland V; Larsson M; Storm G;Östman A; Sandström P; Prakash J MicroRNA-199a and-214 as Potential Therapeutic Targets in Pancreatic Stellate Cells in Pancreatic Tumor. Oncotarget 2016, 7, 16396–16408. [PubMed: 26918939]

(30). Ho AS; Huang X; Cao H; Christman-Skieller C; Bennewith K; Le Q-T; Koong AC Circulating MiR-210 as A Novel Hypoxia Marker in Pancreatic Cancer. Transl. Oncol 2010, 3, 109–113. [PubMed: 20360935]

(31). Huang X; Le Q-T; Giaccia AJ MiR-210–Micromanager of the Hypoxia Pathway. Trends Mol. Med 2010, 16, 230–237. [PubMed: 20434954]

(32). Collins MA; Bednar F; Zhang Y; Brisset J-C; Galbán S; Galbán CJ; Rakshit S; Flannagan KS; Adsay NV; di Magliano MP Oncogenic Kras is Required for Both the Initiation and Maintenance of Pancreatic Cancer in Mice. J. Clin. Invest 2012, 122, 639–653. [PubMed: 22232209]

(33). Collins MA; Brisset J-C; Zhang Y; Bednar F; Pierre J; Heist KA; Galbán CJ; Galbán S; di Magliano MP Metastatic Pancreatic Cancer is Dependent on Oncogenic Kras in Mice. PLoS One 2012, 7, No. e49707. [PubMed: 23226501]

(34). Ying H; Kimmelman AC; Lyssiotis CA; Hua S; Chu GC; Fletcher-Sananikone E; Locasale JW; Son J; Zhang H; Coloff JL; et al. Oncogenic Kras Maintains Pancreatic Tumors through Regulation of Anabolic Glucose Metabolism. Cell 2012, 149, 656–670. [PubMed: 22541435]

(35). Ostrem JM; Shokat KM Direct Small-Molecule Inhibitors of KRAS: from Structural Insights to Mechanism-Based Design. Nat. Rev. Drug Discovery 2016, 15, 771–785. [PubMed: 27469033]

(36). Kamerkar S; LeBleu VS; Sugimoto H; Yang S; Ruivo CF; Melo SA; Lee JJ; Kalluri R Exosomes Facilitate Therapeutic Targeting of Oncogenic KRAS in Pancreatic Cancer. Nature 2017, 546, 498–503. [PubMed: 28607485]

(37). Lo JH; Hao L; Muzumdar MD; Raghavan S; Kwon EJ; Pulver EM; Hsu F; Aguirre AJ; Wolpin BM; Fuchs CS; et al. iRGD-Guided Tumor-Penetrating Nanocomplexes for Therapeutic SiRNA Delivery to Pancreatic Cancer. Mol. Cancer Ther 2018, 17, 2377–2388. [PubMed: 30097486]

(38). Sleightholm RL; Neilsen BK; Li J; Steele MM; Singh RK; Hollingsworth MA; Oupicky D Emerging Roles of the CXCL12/CXCR4 Axis in Pancreatic Cancer Progression and Therapy. Pharmacol. Ther 2017, 179, 158–170. [PubMed: 28549596]

(39). Feig C; Jones JO; Kraman M; Wells RJ; Deonarine A; Chan DS; Connell CM; Roberts EW; Zhao Q; Caballero OL; et al. Targeting CXCL12 from FAP-Expressing Carcinoma-Associated Fibroblasts Synergizes with Anti–PD-L1 Immunotherapy in Pancreatic Cancer. Proc. Natl. Acad. Sci. U. S. A 2013, 110, 20212–20217. [PubMed: 24277834]

(40). Chen Y; Ramjiawan RR; Reiberger T; Ng MR; Hato T; Huang Y; Ochiai H; Kitahara S; Unan EC; Reddy TP; et al. CXCR4 Inhibition in Tumor Microenvironment Facilitates Anti-Programmed Death Receptor-1 Immunotherapy in Sorafenib-Treated Hepatocellular Carcinoma in Mice. Hepatology 2015, 61, 1591–1602. [PubMed: 25529917]

(41). Saur D; Seidler B; Schneider G; Algül H; Beck R; Senekowitsch-Schmidtke R; Schwaiger M; Schmid RM CXCR4 Expression Increases Liver and Lung Metastasis in A Mouse Model of Pancreatic Cancer. Gastroenterology 2005, 129, 1237–1250. [PubMed: 16230077]

(42). Wang Y; Kumar S; Rachagani S; Sajja BR; Xie Y; Hang Y; Jain M; Li J; Boska MD; Batra SK; et al. Polyplex-Mediated Inhibition of Chemokine Receptor CXCR4 and Chromatin-Remodeling Enzyme NCOA3 Impedes Pancreatic Cancer Progression and Metastasis. Biomaterials 2016, 101, 108–120. [PubMed: 27267632]

(43). Li J; Zhu Y; Hazeldine ST; Li C; Oupický D Dual-Function CXCR4 Antagonist Polyplexes to Deliver Gene Therapy and Inhibit Cancer Cell Invasion. Angew. Chem 2012, 124, 8870–8873.

(44). Xie Y; Wang Y; Li J; Hang Y; Oupický D Promise of Chemokine Network-Targeted Nanoparticles in Combination Nucleic Acid Therapies of Metastatic Cancer. Wiley Interdisciplinary Reviews: Wiley Interdiscip. Rev. Nanomed. Nanobiotechnol 2019, 11, No. e1528.

(45). Wang Y; Li J; Chen Y; Oupický D Balancing Polymer Hydrophobicity for Ligand Presentation and SiRNA Delivery in Dual Function CXCR4 Inhibiting Polyplexes. Biomater. Sci 2015, 3, 1114–1123. [PubMed: 26146552]

(46). Xie Y; Wang Y; Li J; Hang Y; Jaramillo L; Wehrkamp CJ; Phillippi MA; Mohr AM; Chen Y; Talmon GA; et al. Cholangiocarcinoma Therapy with Nanoparticles that Combine Downregulation of MicroRNA-210 with Inhibition of Cancer Cell Invasiveness. Theranostics 2018, 8, 4305–4320. [PubMed: 30214622]

(47). Tenzer S; Docter D; Kuharev J; Musyanovych A; Fetz V; Hecht R; Schlenk F; Fischer D; Kiouptsi K; Reinhardt C; et al. Rapid Formation of Plasma Protein Corona Critically Affects Nanoparticle Pathophysiology. Nat. Nanotechnol 2013, 8, 772–781. [PubMed: 24056901]

(48). Deng Y; Yang F; Cocco E; Song E; Zhang J; Cui J; Mohideen M; Bellone S; Santin AD; Saltzman WM Improved IP Drug Delivery with Bioadhesive Nanoparticles. Proc. Natl. Acad. Sci. U. S. A 2016, 113, 11453–11458. [PubMed: 27663731]

(49). Bajaj G; Yeo Y Drug Delivery Systems for Intraperitoneal Therapy. Pharm. Res 2010, 27, 735–738. [PubMed: 20198409]

(50). Hirano K; Hunt CA Lymphatic Transport of Liposome-Encapsulated Agents: Effects of Liposome Size Following Intraperitoneal Administration. J. Pharm. Sci 1985, 74, 915–921. [PubMed: 4067845]

(51). Meng F; Wang J; Ping Q; Yeo Y Quantitative Assessment of Nanoparticle Biodistribution by Fluorescence Imaging, Revisited. ACS Nano 2018, 12, 6458–6468. [PubMed: 29920064]

(52). Yuan W; Yang D; Su Q; Zhu X; Cao T; Sun Y; Dai Y; Feng W; Li F Intraperitoneal Administration of Biointerface-Camouflaged Upconversion Nanoparticles for Contrast Enhanced Imaging of Pancreatic Cancer. Adv. Funct. Mater 2016, 26, 8631–8642.

(53). Knockenhauer KE; Schwartz TU The Nuclear Pore Complex as A Flexible and Dynamic Gate. Cell 2016, 164, 1162–1171. [PubMed: 26967283]

(54). Ernsting MJ; Murakami M; Roy A; Li S-D Factors Controlling the Pharmacokinetics, Biodistribution and Intratumoral Penetration of Nanoparticles. J. Controlled Release 2013, 172, 782–794.

(55). Kamei T; Kitayama J; Yamaguchi H; Soma D; Emoto S; Konno T; Ishihara K; Ishigami H; Kaisaki S; Nagawa H Spatial Distribution of Intraperitoneally Administrated Paclitaxel Nanoparticles Solubilized with Poly (2-Methacryloxyethyl Phosphorylcholine-co n-Butyl Methacrylate) in Peritoneal Metastatic Nodules. Cancer Sci. 2011, 102, 200–205. [PubMed: 20942868]

(56). Nichols JW; Bae YH EPR: Evidence and Fallacy. J. Controlled Release 2014, 190, 451–464.

(57). Wayne EC; Long C; Haney MJ; Batrakova EV; Leisner TM; Parise LV; Kabanov AV Targeted Delivery of SiRNA Lipoplexes to Cancer Cells Using Macrophage Transient Horizontal Gene Transfer. Adv. Sci 2019, 6, 1900582.

(58). Liu X; Lin P; Perrett I; Lin J; Liao Y-P; Chang CH; Jiang J; Wu N; Donahue T; Wainberg Z; et al. Tumor-Penetrating Peptide Enhances Transcytosis of Silicasome-Based Chemotherapy for Pancreatic Cancer. J. Clin. Invest 2017, 127, 2007–2018. [PubMed: 28414297]

(59). Orimo A; Gupta PB; Sgroi DC; Arenzana-Seisdedos F; Delaunay T; Naeem R; Carey VJ; Richardson AL; Weinberg RA Stromal Fibroblasts Present in Invasive Human Breast Carcinomas Promote Tumor Growth and Angiogenesis through Elevated SDF-1/CXCL12 Secretion. Cell 2005, 121, 335–348. [PubMed: 15882617]

(60). Turley SJ; Cremasco V; Astarita JL Immunological Hallmarks of Stromal Cells in the Tumour Microenvironment. Nat. Rev. Immunol 2015, 15, 669–682. [PubMed: 26471778]

(61). Chen IX; Chauhan VP; Posada J; Ng MR; Wu MW; Adstamongkonkul P; Huang P; Lindeman N; Langer R; Jain RK Blocking CXCR4 Alleviates Desmoplasia, Increases T-lymphocyte Infiltration, and Improves Immunotherapy in Metastatic Breast Cancer. Proc. Natl. Acad. Sci. U. S. A 2019, 116, 4558–4566. [PubMed: 30700545]

(62). Wang H; Flach H; Onizawa M; Wei L; McManus MT; Weiss A Negative Regulation of Hif1a Expression and T_H17 Differentiation by the Hypoxia-Regulated MicroRNA MiR-210. Nat. Immunol 2014, 15, 393–401. [PubMed: 24608041]

(63). Miao L; Li J; Liu Q; Feng R; Das M; Lin CM; Goodwin TJ; Dorosheva O; Liu R; Huang L Transient and Local Expression of Chemokine and Immune Checkpoint Traps to Treat Pancreatic Cancer. ACS Nano 2017, 11, 8690–8706. [PubMed: 28809532]

(64). Beider K; Bitner H; Leiba M; Gutwein O; Koren-Michowitz M; Ostrovsky O; Abraham M; Wald H; Galun E; Peled A; et al. Multiple Myeloma Cells Recruit Tumor-Supportive Macrophages through the CXCR4/CXCL12 Axis and Promote Their Polarization toward the M2 Phenotype. Oncotarget 2014, 5, 11283–11296. [PubMed: 25526031]

(65). Zhang B; Karrison T; Rowley DA; Schreiber H IFN-γ–and TNF-Dependent Bystander Eradication of Antigen-Loss Variants in Established Mouse Cancers. J. Clin. Invest 2008, 118, 1398–1404. [PubMed: 18317595]

(66). Milanovic M; Fan DNY; Belenki D; Dabritz JHM; Zhao Z; Yu Y; Dörr JR; Dimitrova L; Lenze D; Barbosa IAM; et al. Senescence Associated Reprogramming Promotes Cancer Stemness. Nature 2018, 553, 96–100. [PubMed: 29258294]

(67). Intartaglia M; Sabetta R; Gargiulo M; Roncador G; Marino FZ; Franco R Immunohistochemistry for Cancer Stem Cells Detection: Principles and Methods. Methods Mol. Biol 2018, 1692, 195–211. [PubMed: 28986898]

(68). Stathis A; Moore MJ Advanced Pancreatic Carcinoma: Current Treatment and Future Challenges. Nat. Rev. Clin. Oncol 2010, 7, 163–172. [PubMed: 20101258]

(69). Morano W; Aggarwal A; Love P; Richard S; Esquivel J; Bowne W Intraperitoneal Immunotherapy: Historical Perspectives and Modern Therapy. Cancer Gene Ther 2016, 23, 373–381. [PubMed: 27834358]

(70). Levine EA; Votanopoulos KI; Shen P; Russell G; Fenstermaker J; Mansfield P; Bartlett D; Stewart JH A Multicenter Randomized Trial to Evaluate Hematologic Toxicities after Hyperthermic Intraperitoneal Chemotherapy with Oxaliplatin or Mitomycin in Patients with Appendiceal Tumors. J. Am. Coll. Surg 2018, 226, 434–443. [PubMed: 29331663]

(71). Levine EA; Stewart JH IV; Shen P; Russell GB; Loggie BL; Votanopoulos KI Intraperitoneal Chemotherapy for Peritoneal Surface Malignancy: Experience with 1,000 Patients. J. Am. Coll. Surg 2014, 218, 573–585. [PubMed: 24491244]

(72). Thadi A; Khalili M; Morano W; Richard S; Katz S; Bowne W Early Investigations and Recent Advances in Intraperitoneal Immunotherapy for Peritoneal Metastasis. Vaccines 2018, 6, 54.

(73). Katz S; Point GR; Cunetta M; Thorn M; Guha P; Espat NJ; Boutros C; Hanna N; Junghans RP Regional CAR-T Cell Infusions for Peritoneal Carcinomatosis Are Superior to Systemic Delivery. Cancer Gene Ther 2016, 23, 142–148. [PubMed: 27080226]

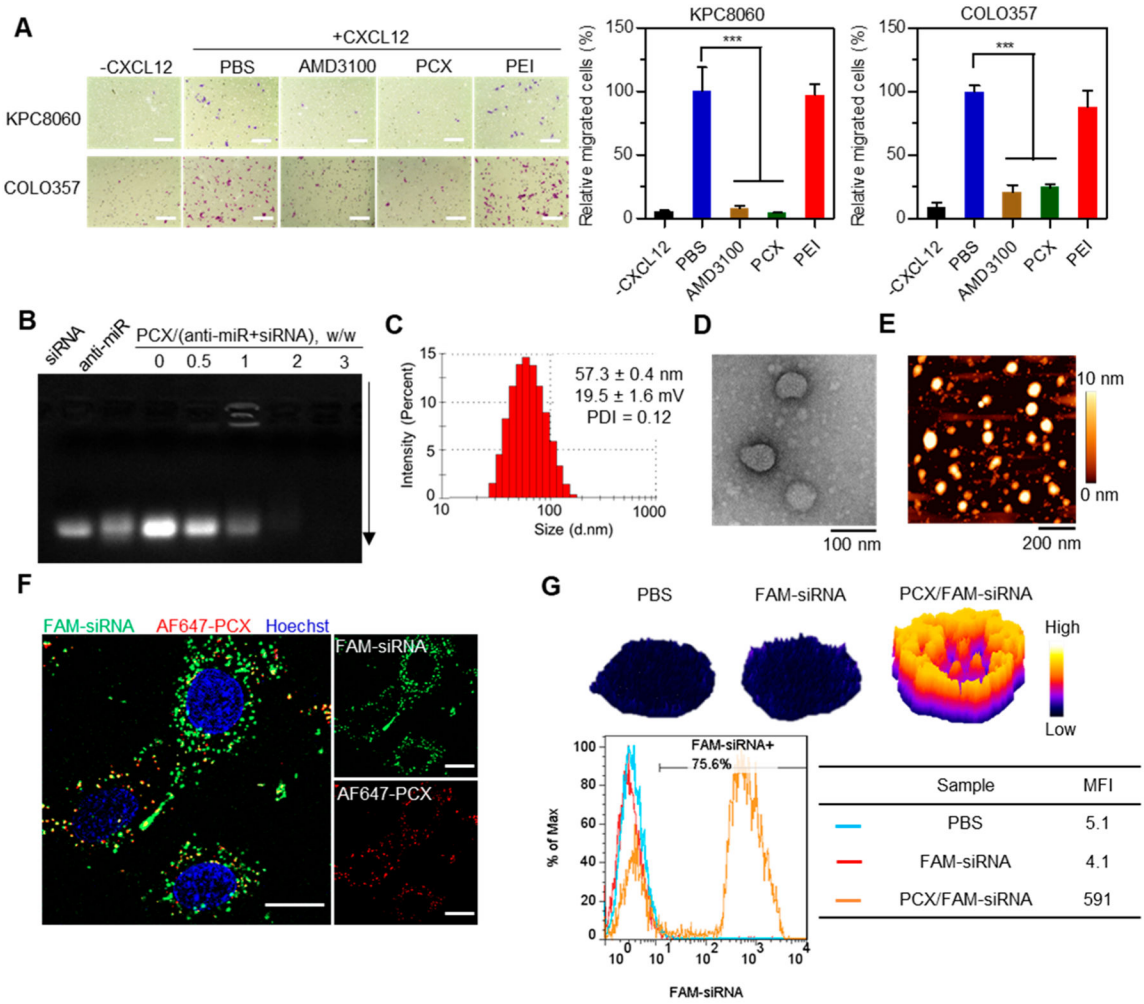

Figure 1.

PCX inhibits CXCR4 and delivers anti-miR/siRNA combination *in vitro*. (A) Inhibition of CXCL12-induced PDAC cell migration. KPC8060 and COLO357 cells were treated with AMD3100 (300 nM), PCX (2 μg/mL), or PEI (2 μg/mL) and cultured in a transwell membrane insert (3×10^5 cells) with CXCL12 (20 nM) as chemoattractant. Migrated cells were observed under a microscope. Scale bar, 200 μm. Data are shown as mean ± SD (n = 3). ***$P < 0.001$. (B) Analysis of the condensation of anti-miR and siRNA by PCX using agarose gel electrophoresis (equal molar ratio of anti-miR and siRNA). (C) Measurement of hydrodynamic size of PCX/(anti-miR+siRNA) nanoparticles (w/w = 2) by dynamic light scattering. (D) TEM and (E) AFM images of PCX/(anti-miR+siRNA) nanoparticles (w/w = 2). (F) Confocal microscopy observation of KPC8060 cells after treatment with AF647-PCX/FAM-siRNA nanoparticles for 4 h. Scale bar, 20 μm. (G) Surface plot of KPC8060 multicellular spheroids after treatment with free FAM-siRNA or PCX/FAM-siRNA for 12 h. Flow cytometry analysis of KPC8060 cells digested from multicellular spheroids.

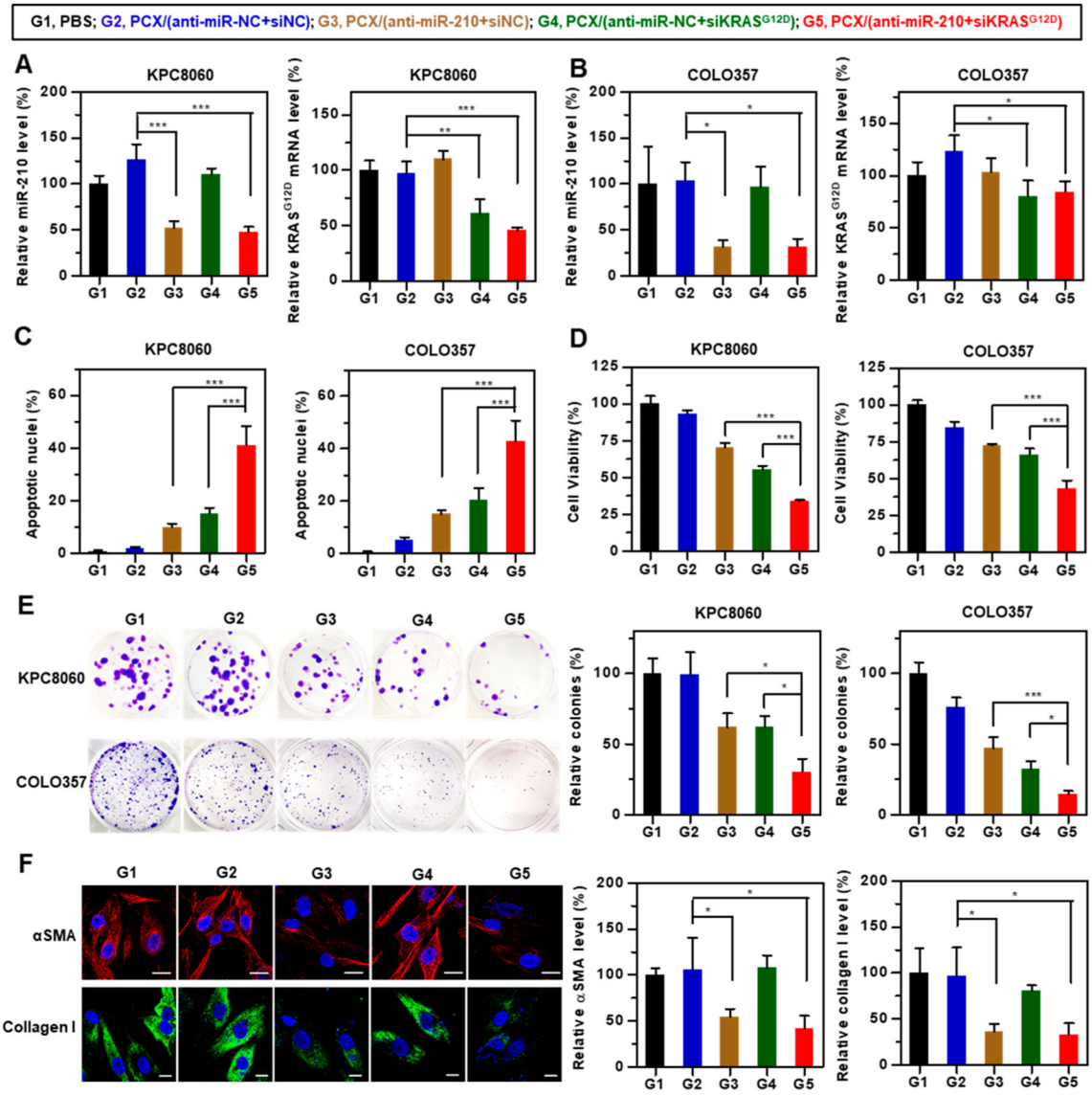

Figure 2.

Nanoparticles inhibited both pancreatic cancer cells and PSCs *in vitro*. (A) Levels of miR-210 and $KRAS^{G12D}$ mRNA in KPC8060 cancer cells after treatment with PCX nanoparticles (50 nM anti-miR, 50 nM siRNA) for 48 h. (B) Levels of miR-210 and $KRAS^{G12D}$ mRNA in COLO357 cancer cells after treatment with PCX nanoparticles (50 nM anti-miR, 50 nM siRNA) for 48 h. (C) Cell apoptosis assay by DAPI staining. (D) Cell viability assay by CellTiterBlue after PCX nanoparticles treatment (50 nM anti-miR, 50 nM siRNA) for 48 h. (E) Colony formation assay of cells after treatment by nanoparticles. (F) Immunofluorescence staining of αSMA and collagen I in human PSCs after treatment with PCX nanoparticles (50 nM anti-miR, 50 nM siRNA) for 48 h. The relative expression levels (mean fluorescence intensity) of fibrosis marker were quantified using ImageJ software. Data are shown as mean ± SD ($n = 3$). *$P < 0.05$, **$P < 0.01$, ***$P < 0.001$.

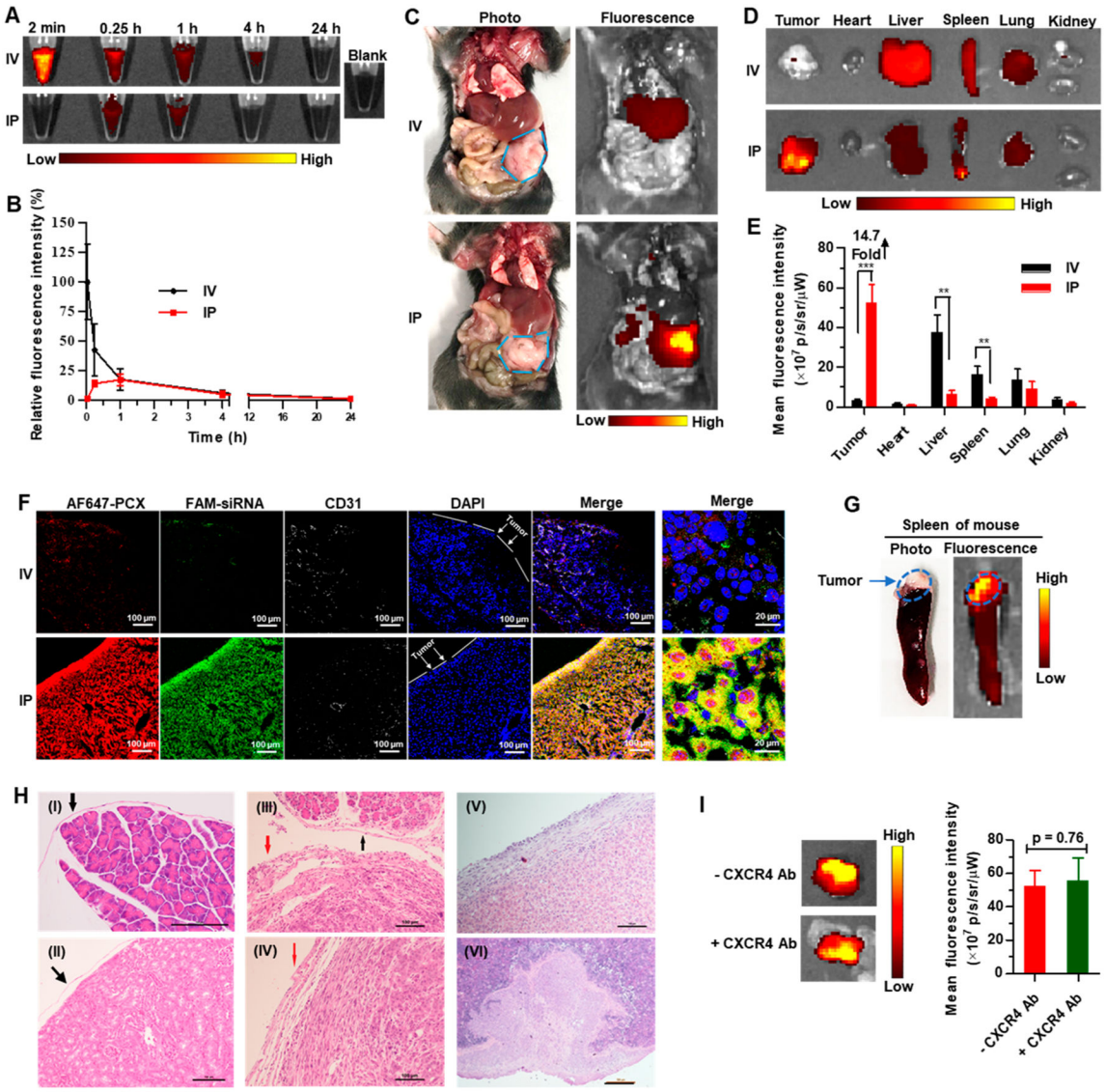

Figure 3.

Improved delivery of nanoparticles to orthotopic pancreatic tumor/metastasis through IP administration. Orthotopic pancreatic tumor-bearing mouse-derived from KPC8060 cells were administered with the same dose of AF647-PCX/FAM-siRNA nanoparticles (5 mg/kg AF647-PCX, 2.5 mg/kg FAM-siRNA) via IV or IP injection. (A) Blood fluorescence (AF647) over time after IV or IP injection. Blood was drawn from mice after IV or IP injection with AF647-PCX/FAM-siRNA nanoparticles at various times and imaged under a fluorescence imaging system (Ex = 640 nm, Em = 680 nm). The fluorescence intensity at 2 min in the IV group was set as 100%. Results are expressed as relative fluorescence intensity ± SD ($n = 3$). (B) Curves of relative fluorescence intensity in blood over time. (C) Biodistribution of AF647-PCX/FAM-siRNA nanoparticles in mice at 24 h after injection. Mice were sacrificed and imaged using a fluorescence imaging system (Ex = 640 nm, Em = 680 nm). Photos of mice were also taken (circles indicate tumor). (D) *Ex vivo* fluorescence images of the tumors and tissues at 24 h after injection. (E) Semiquantitative analysis of

fluorescence intensity in the tumors and tissues. Results are expressed as mean fluorescence intensity ± SD ($n = 3$). $^{**}P < 0.01$, $^{***}P < 0.001$.(F) Confocal microscopy images of frozen tumor sections at 24 h after injection. PCX is shown in red (AF647), siRNA in green (FAM), blood vessels in white (Cy3), and the nuclei in blue (DAPI). (G) Distribution of nanoparticles in the spleen with tumor invasion at 24 h after IP injection. *Ex vivo* fluorescence images of spleens were taken using Ex = 640 nm, Em = 680 nm. Photos of spleen were also taken (circles indicated tumor). (H) HE staining of (I) normal pancreas with mesothelial lining (black arrow), scale bar = 100 μm, (II) normal kidney (without metastasis) with mesothelial lining (black arrow), scale bar = 100 μm, (III) normal pancreas with mesothelium (black arrow) and tumor with capsule (red arrow) but no mesothelium in single section, scale bar = 100 μm, (IV) primary pancreatic tumor with capsule (red arrow) but no mesothelium, scale bar = 100 μm, (V) liver metastasis without mesothelium, scale bar = 100 μm, (VI) spleen metastasis without mesothelium, scale bar = 500 μm. (I) Comparison of the distribution of nanoparticles in the tumor at 24 h after IP injection in mice with/without pretreatment with the anti-CXCR4 antibody.

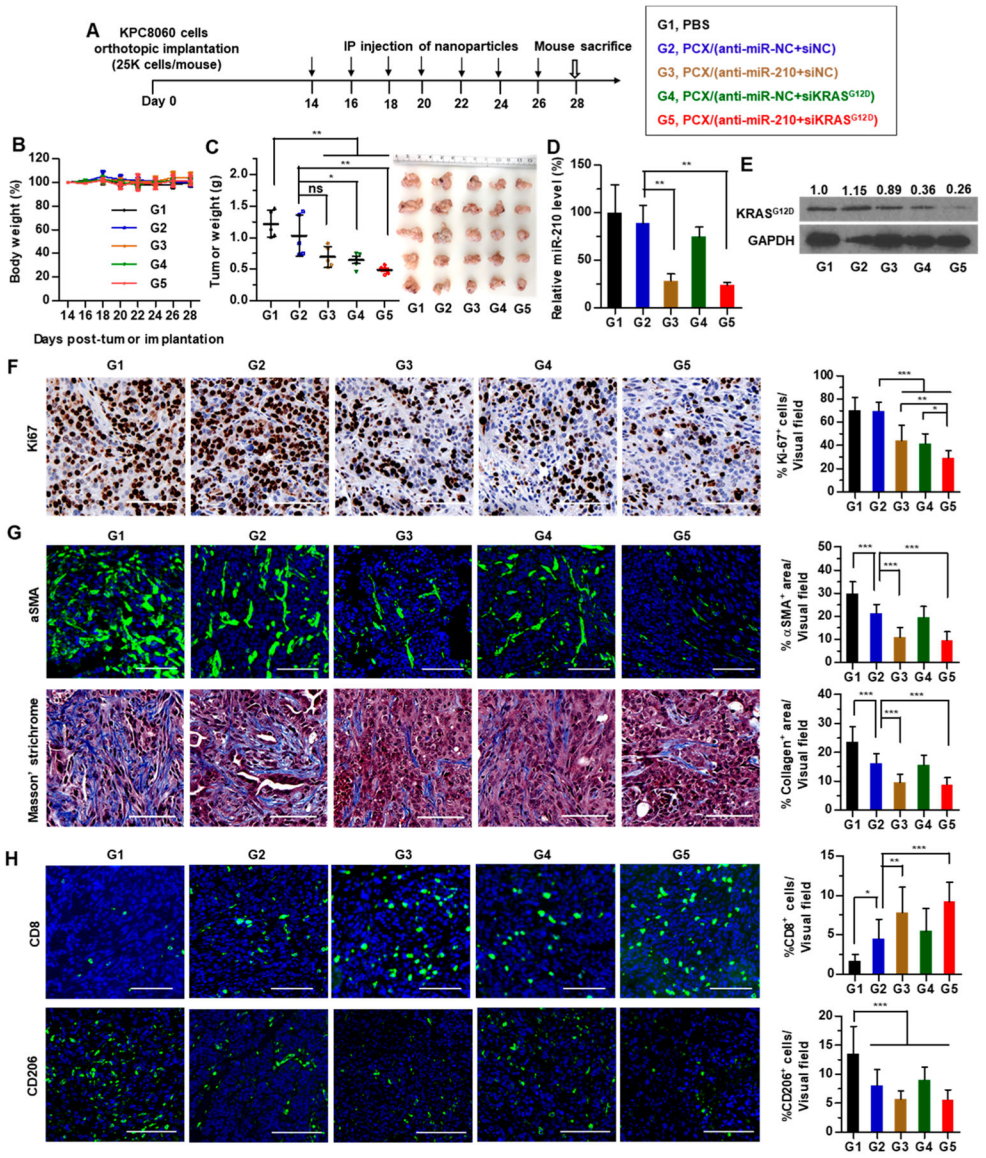

Figure 4.

IP delivery of nanoparticles reduced stromal desmoplasia without induction of immunosuppression for orthotopic pancreatic cancer treatment. (A) Orthotopic tumor-bearing mice received multiple IP injections of PCX/(anti-miR+siRNA) nanoparticles (5 mg/kg PCX). (B) Relative mouse body weight (%) during treatment. (C) Weight of the primary tumor from the mouse after treatment. Data are shown as mean ± SD (n = 5). (D) Levels of miR-210 in tumors after treatment analyzed by qRT-PCR analysis. Data are shown as mean ± SD (n = 3). (E) Expression of KRAS^{12D} in tumors after treatment analyzed by Western blot. (F) Immunohistochemistry analysis of K_i-67 in tumors after treatment. Scale bar = 100 μm. (G) Tumor-associated fibrosis analysis in tumors after treatment. Masson's trichrome staining and αSMA immunofluorescence analysis (shown as green) in tumors after treatment. Scale bar = 100 μm. αSMA$^+$ or collagen$^+$ area (percentage) in each field was quantified by ImageJ software. (H) Immunofluorescence analysis of CD8$^+$ and CD206$^+$

(shown as green) in tumors after treatment. Scale bar = 100 μm. Twelve to fifteen visual fields were randomly captured from three tumor sections in five mice per each group for quantification. Data are shown as mean ± SD *P < 0.05, **P < 0.01, ***P < 0.001.

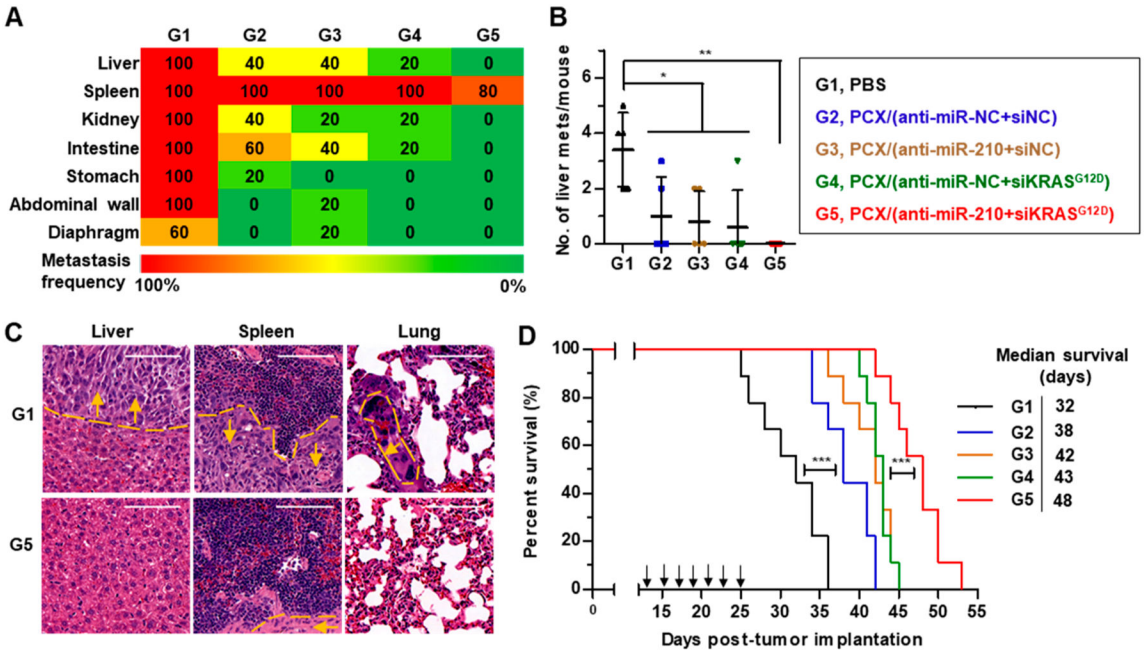

Figure 5.

IP delivery of nanoparticles inhibited metastasis and improved survival in orthotopic pancreatic cancer-bearing mice. (A) Heat map of tumor metastasis frequency in tissues and organs. (B) Macroscopic metastatic nodules in the liver after treatment. Data are shown as mean ± SD ($n = 5$). *$P < 0.05$, **$P < 0.01$. (C) HE analysis of metastasis in tissues/organs. (D) Kaplan–Meier survival graph of orthotopic pancreatic tumor-bearing mice after treatment. Arrows indicate injections of nanoparticles. Nine mice per group. Log-rank Mantel-Cox test, ***$P < 0.001$.

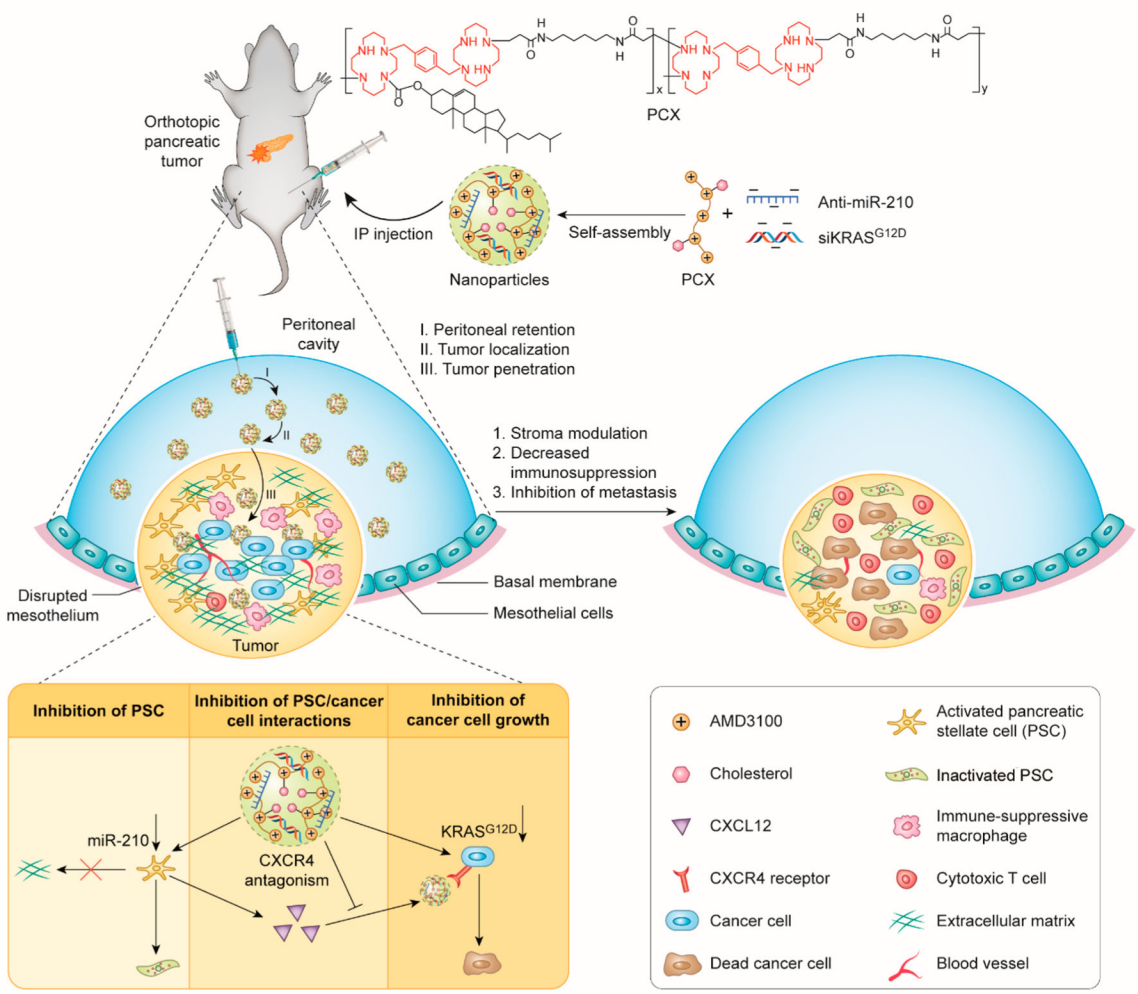

Scheme 1.

Proposed Mechanism of EPR-Independent Delivery of miRNA/siRNA Nanotherapy in Pancreatic Cancer Treatment[a]

[a]IP administration delivers PCX nanoparticles to orthotopic pancreatic tumor in an EPR-independent manner. PCX nanoparticles are retained in the peritoneal cavity, localize to peritoneal tumors lacking surface mesothelium, and penetrate deep into tumor. The nanoparticles modulate desmoplastic stroma, reduce immune suppression, and inhibit metastasis through simultaneously inactivating PSCs, inhibiting cancer cells, and blocking cancer–stroma interaction.